2013

Premelting Study of Nickel Nanorod Arrays

Ebtihaj Alrashid Jr.
Virginia Commonwealth University

Premelting Study of Nickel Nanorod Arrays

A thesis submitted in partial fulfillment of the requirements for the degree of Master of Science in Physics / Applied Physics at Virginia Commonwealth University.

By

Ebtihaj Alrashid

B.S. in Physics

King Faisal University, 2006

M.S. in Physics/Applied Physics

Virginia Commonwealth University, 2013

Director:

Dr. Dexian Ye, Assistant Professor, Department of Physics

Virginia Commonwealth University

Richmond, Virginia, 23220

May 1, 2013

Acknowledgments

First and foremost, my utmost gratitude to my GOD for blessing me everything that makes my life harmonious. Secondly, I would like to express my deepest thankful to my parents who encourage me and support me to do the best in every step in my life from early age to be the parson who I am today. I always look at them as the best role models as parents and professional people to simulate in my life. Sincere thanks goes to my brothers and sisters for their love, courtesy, and encouragements, especially my brother, Basil, who helped me writing my thesis on the computer successfully, without him, my thesis was not done.

I am forever indebted and appreciative towards my husband who motivated me to complete my education to achieve my goals. My life would be less worth living if not for him. He sacrificed much of his efforts and his time caring my children and providing me needed support. Further, all my love and appreciation to him and my lovely kids for their patience during my studying time in school. All thankfulness goes to all my friends in my home country and U.S. for their kindness and encouragements.

This thesis would not have been achieved successfully without the help and guidance from my academic advisor, Dr. Dexian Ye. I can't say thank you enough for his tremendous support and help in my experiments as well as writing my thesis. I would like to express my thanks to my committee members, Dr. Maryanne Collinson and Dr. Reshchikov, for their useful comments. I acknowledge and thank Dr. Dmitry Pestov for his training on the SEM instrument. A great thankfulness goes to all Physics faculty, staff, and students in Physics department at VCU. Many thanks towards Saudi Arabia government for their support.

Last but not least, I dedicate this work to my husband, Ahmed. Everything I've done here in U.S. I did for you.

Table of Contents

List of Figures

List of Tables

Abstract

Premelting Study of Nickel Nanorod Arrays

By Ebtihaj Alrashid

A thesis submitted in partial fulfillment of the requirements for the degree of Master of Science at Virginia Commonwealth University. Virginia Commonwealth University, 2013.

Major Director: Dr. Dexian Ye, Assistant Professor, Department of Physics/Applied Physics

In this study, samples of nanoscale structures of nickel (Ni) nanorods were prepared using the glancing angle deposition (GLAD) technique. Annealing was done using a split- top tube furnace at high vacuum chamber pressure. The pre-melting of the nanorods was maintained at 500 °C for 30 minutes in all the samples. Using the samples with 90 minutes of GLAD time, the annealing behavior of the nanorods was studied at 300 °C, 400 °C, 500 °C and 600 °C. The nanorods were then imaged using scanning electron microscopy. Using X-ray diffraction, the crystalline microstructures of the nanorods were studied. It was found that with increasing annealing temperatures, the intensity of peaks for both Ni (111) and Ni (200) increased, which indicates that better crystals were formed. The results indicate that re-crystallization occurs after annealing, leading to the formation of larger grain sizes compared to as-deposited grain sizes. Annealing substantially changed the structure of the nanorods, leading to different smoother, more connected crystal structures for the annealed nanorods compared to as-deposited ones.

Chapter 1: Introduction and Motivation

Nickel nanorods are of interest in various fields of study owing to the fascinating attributes they have. The nanorods might find applications in fields as far apart as composites, solar energy, fuel cells and in electronics.[1] The nanorods have magnetic properties, which can be utilized in magnetic recording, and they have superb catalytic activities.[1] They can be used as nanowires in circuits as well as being additives in fabrics.[1] The magnetic and conducting properties of nickel nanorods make them excellent materials in medical applications such as in medical sensors and biomedicine.[1]

Random deposits of nickel exhibits high magnetic anisotropy, with periodic deposits exhibiting isotropic magnetic properties.[1] Since the order in which nickel particles are deposited on a given material dictates their magnetic properties, different types of deposits can be utilized for various purposes. Annealing is often done to change the physical properties of metals. In this study, the influence of annealing on prepared nanorods of nickel is examined. The nanorods were created using (GLAD) technique and then samples were annealed at varying temperatures. The resulting structures were analyzed using X-ray diffraction (XRD) and scanning electron microscopy (SEM). SEM was used to discover the morphology change that had occurred.

By furthering research into the behavior of nickel nanorods and improving knowledge on the structures it forms, it is possible to advance technology. The study focuses on the thermodynamic properties of nickel nanorods by examining how they behave under different temperatures. The structures and behavior of nickel nanorods after being subjected to different thermodynamic conditions will offer insights into potential properties and uses for the substance. For example, the substance could be prepared to increase surface area in areas that require catalysis or improve its crystalline structure to improve its strength. This study may also allow

for inferences to be made about the best temperature to work in, which, combined with the polar and azimuthal plane of the substrate, can produce different typographies of the substance.

Graphene, a material that is of considerable interest to scientists, has been successfully grown on copper and nickel foils.[2] Graphene that was grown on nickel showed some promise in the improvement of battery performance.[2] This is because the material was able to store and let loose lithium ions more effectively.[2] In addition, using a graphene-nickel cobaltite nanocomposite, an asymmetric electrochemical supercapacitor has been made.[3] If one can deposit graphene-nickel nanocomposite through annealing, the electrodes for supercapacitor can be manufactured in a cost efficient and scalable fashion.

Chapter 2: X-Ray Diffraction

XRD is among the principal tool for studying materials in nanotechnology world. XRD was invented in 1912-1913 when the English physicists William Henry Bragg and his son William Lawrence Bragg developed Bragg's Law to explain the phenomena of the cleavage faces of crystals that appears to reflect x-ray beams at certain angles of incidence.[4] The Braggs were awarded the 1915 Nobel Prize in Physics for their invention in crystallography. The Bragg's Law invention confirmed the idea that x-rays is a form of electromagnetic radiation. [5,6] The first crystal structure was determined in 1914 by Braggs when they discovered the atomic structure of rock salt (NaCl), ZnS, and diamond.[7,8,9]

Historically, XRD was evolved in different time periods by various groups of scientists. The utility of XRD has been developed to investigate the structures of the crystals in all states of matter with any beam (e.g. ions, protons, electrons, and neutrons) with a wavelength in the scope of the distance between the atomic or molecular structures of interest.[10]

2.1 The Principle of X–Ray Diffraction:

X-rays are electromagnetic radiation with wavelengths from about 10^{-2} to 10^{2} Å (1 Å = 10^{-10} meters)[10]. X-rays, like light, propagate with the velocity of light c by

$$\lambda = \frac{c}{\upsilon} \tag{2.1}$$

where λ is the wavelength of the waves and υ is the frequency, and $c = 2.998 \times 10^{8}$ m/s. Thus, the energy of x-rays as a form of electromagnetic radiation is proportional to the wavelength which is related to each other by Einstein's equation:

$$E = h\upsilon = hc / \lambda \tag{2.2}$$

where E is the energy of the x-rays and h is the Plank's constant which is 6.62517×10^{-27} erg.sec.[11] Thus, since the x-rays with the wavelengths of around 1 Å have the same order of size as most interatomic distances in crystals, they play the important role in probing the structures of crystals in nanotechnology.[10]

One of the x-rays techniques that are used in nanotechnology is XRD which is a non-destructive detection method.[11] XRD is the scattering of x-rays beam caused by the crystalline atoms to produce the diffraction pattern that yields the information about the structure of the crystals.[12]

2.2 X-Ray Production:

X-rays are produced by accelerating electrons with a high voltage to allow them to collide with a metal target. Some of the electrons with sufficient energy will knock the electron out of an inner shell of the atoms causing the electrons to drop down from higher states to fill the vacancy. That will cause these electrons losing some of their energies and emitting x-ray protons with the energies which can be determined by the electron energy levels.[13]

This phenomenon of x-ray emission happens in an x-rays tube which contains a source of electrons accelerated by a high voltage between the cathode and the anode of tungsten filament, and a metal target (usually, copper) as shown in FIG. 2.1. Furthermore, the x-rays tube is water-cooled to prevent the target from melting.[13]

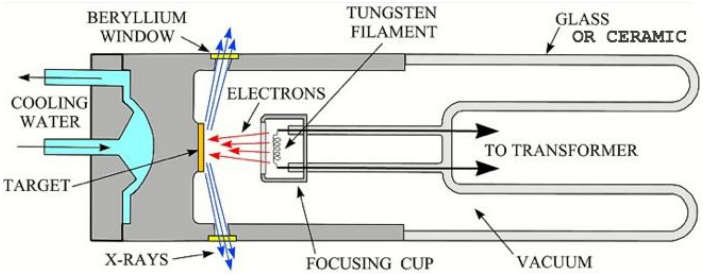

FIG. 2.1: Schematic cross section of an x–ray tube.[14] (Image source: X-Ray Diffraction Primer 2001, Coastal and Marine Geology Program Online, Retrieved 25 February 2013, from http://pubs.usgs.gov/of/2001/of01-041/htmldocs/xrpd.htm)

2.3 Diffractometer Geometries:

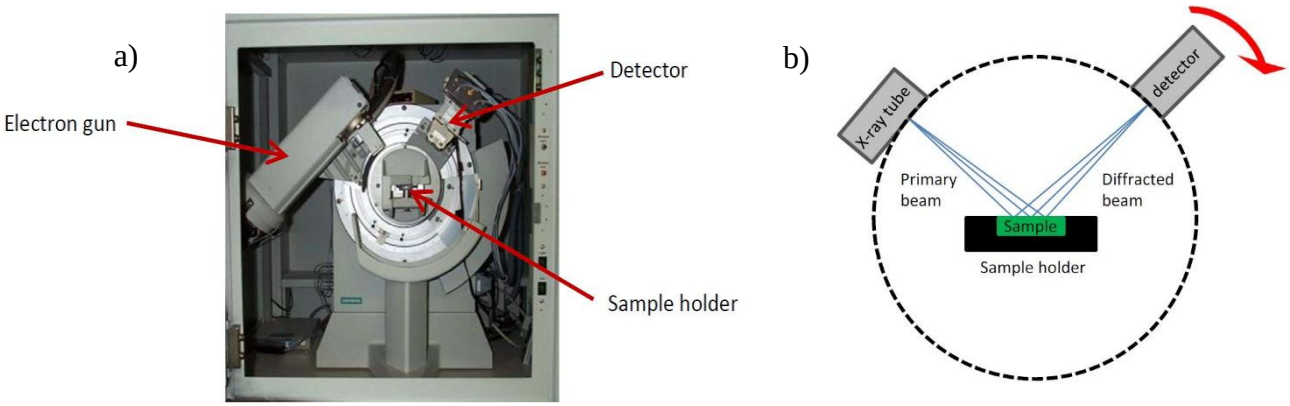

FIG. 2.2: (a) XRD machine**. (**b) Diffractometer geometries.[15] (Image source: Mitchell. S, Pérez-Ramírez. J, X-ray diffraction, Retrieved 1 March, 2013, from http://cc.usst.edu.cn/Download/26da9cdf-6134-41fc-bf56-6dcccd9edd20.pdf)

Figure 2.2 (b) shows the classic reflection geometry which is called Bragg-Brentano geometry. It shows how the x-rays are emitted from the source in the x-ray tube to collide the sample and reflect back by the same angle of incidence, and then it is detected by the detector. This method is recommended for strongly absorbing samples.[12]

2.4 Bragg's Law:

Bragg's law is one of the crucial concepts in XRD which is used in many applications. Bragg's diffraction occurs whenever the wavelength of electromagnetic radiation is comparable

to the repeat distance between the scattering centers. When the x-rays are incident upon the crystal surface, it will scatter in a specular fashion by the atoms in the system and the angle of incidence will reflect back with the same angle of scattering θ. Thus, the constructive interference will occur if the path difference d between two waves is equal to all numbers of wavelengths. That phenomenon helms to Bragg's law which can be written in the form

$$n\lambda = 2d\sin\theta \tag{2.3}$$

where n is the order of reflection, λ is the wavelength of the incident x-rays, d is the spacing of the crystal layers (path difference), and θ is the angle of incidence.[13]

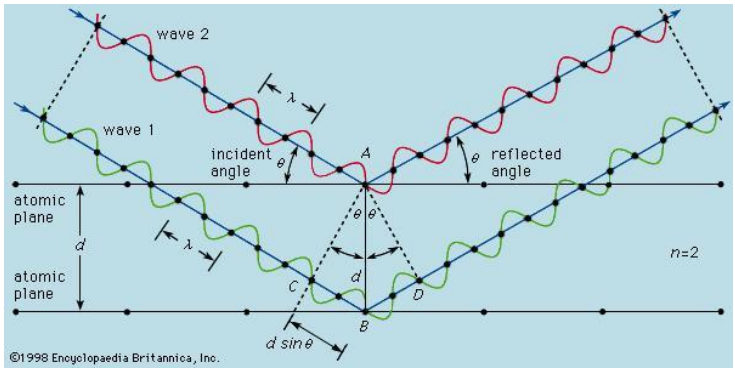

FIG. 2.3: Bragg Diffraction.[16] (Image source: Bragg law 2013. *Encyclopedia Britannica Online*. Retrieved 25 February, 2013, from http://www.britannica.com/EBchecked/topic/76973/Bragg-law)

2.5 XRD Applications:

XRD is a useful tool used to study the structures of nanoscale materials. XRD techniques can be used to:

- Identify the phases and orientation of the crystalline materials.

- Study the structural properties such as lattice parameters, strain, grain size, and thermal expansion.
- Measure the thickness of thin films and multi-layers.
- Determine the arrangement of atoms in crystals.[13]

2.6 Basics of Crystallography:

A crystal is formed by repeating three-dimensional (3D) pattern of the unit cell into a lattice. The unit cell can contain a single atom or atoms in a fixed arrangement. These atoms are arranged in planes with a distance (*d*) and characteristic angles between them. Crystals can be formed into many atomic planes with different *d*-spacing and various sizes and shapes. However, the particular arrangement of the unit cells and the way of their joining is called a crystal lattice.

Each unit cell has *a*, *b*, and *c* which are the lengths of the basis vectors and they are called the lattice constants or parameters. Further, there are three angles *α*, *β* and *γ* between these vectors. *α* can be defined as the angle between *b* and *c*, *β* between *a* and *c*, and *γ* between *a* and *b*.[17]

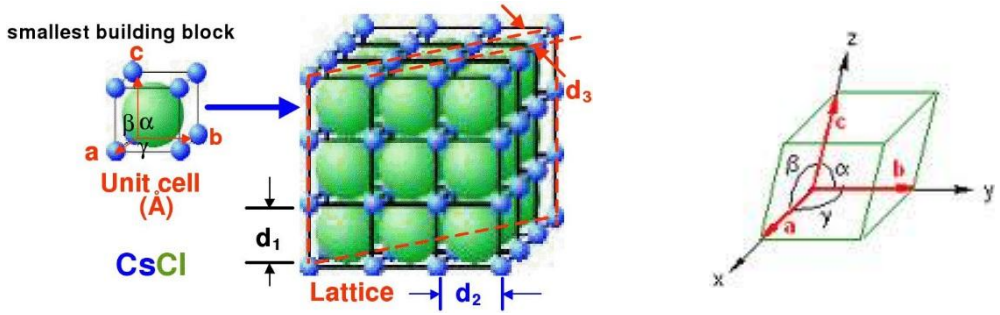

FIG. 2.4: The unit cell in the lattice of crystal's structure[18]

(Image source: http://web.pdx.edu/~pmoeck/phy381/Topic5a-XRD.pdf)

2.7 The Seven Crystal Systems:

According to all possible symmetries for the lattice, there are seven groups of crystal systems. They are defined on the basis geometrical arrangement of the crystal lattice.

Furthermore, there are 14 Bravais lattice types are distributed into the seven lattice systems as shown in the following table[17]:

Table 2. 1: The distribution of the 14 Bravais lattice types into 7 lattice systems (source: http://en.wikipedia.org/wiki/Bravais_lattice)[19]

The 7 lattice systems	The 14 Bravais Lattices			
triclinic (parallelepiped)	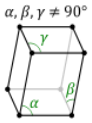			
monoclinic (right prism with parallelogram base; here seen from above)	Simple	base-centered		
	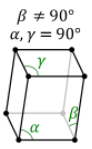	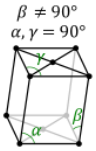		
orthorhombic (cuboid)	simple	base-centered	body-centered	face-centered
	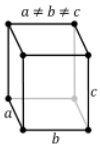	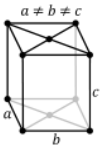	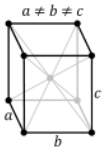	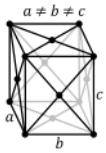
tetragonal (square cuboid)	simple	body-centered		
	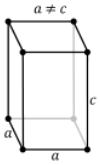	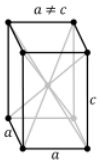		
rhombohedral (trigonal trapezohedron)	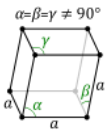			
hexagonal (centered regular hexagon)	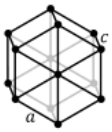			
cubic (isometric; cube)	simple	body-centered	face-centered	
	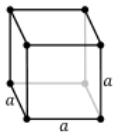	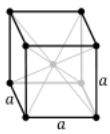	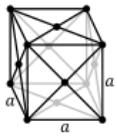	

2.8 Lattice Parameters and Bragg's Law:

To understand the planes of crystals as we will discuss through this thesis, several atomic planes and their *d*-spacing in a simple cubic are shown in FIG. 2.5:

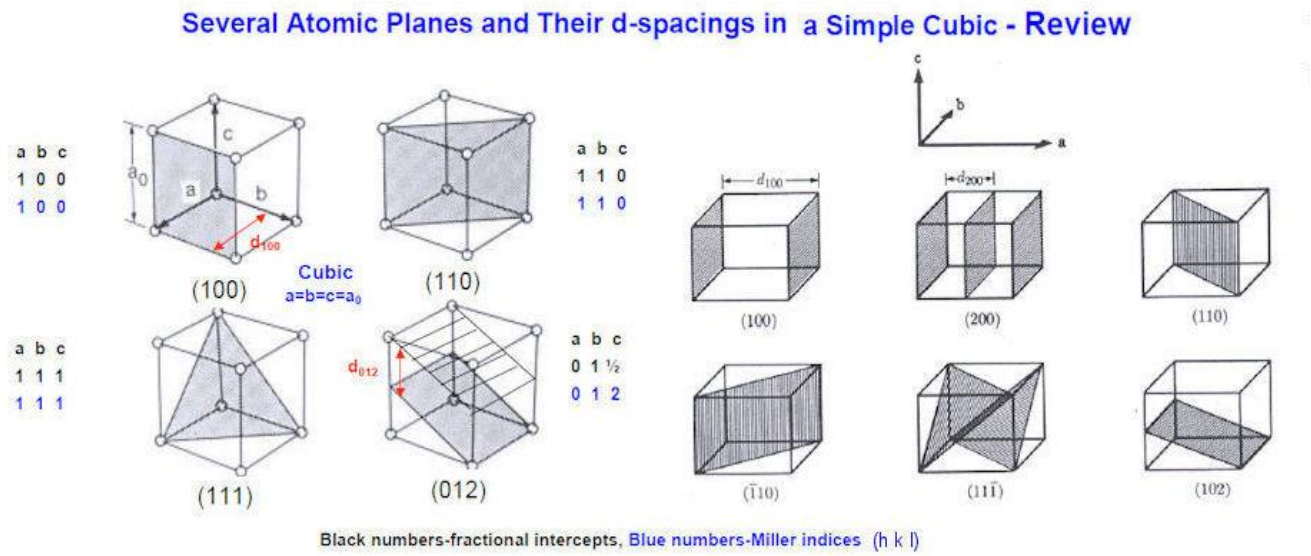

FIG. 2.5: Several atomic planes and their *d*-spacing in a simple cubic.[18]
(Image source: http://web.pdx.edu/~pmoeck/phy381/Topic5a-XRD.pdf).

Measuring the lattice parameters of a crystalline material is one of Bragg's law applications. The dimensions of any unit cell can be found by measuring the path distance in a crystal which is the distance between two parallel atomic planes. This correlation between the lattice parameter a_o and path distance d in a simple cubic structure is defined by:

$$d = \frac{a_o}{\sqrt{h^2 + k^2 + l^2}} \tag{2.4}$$

where h, k, and l are the intercept of the diffracting plane with the x, y, and z – axis respectively.[13]

2.9 Using XRD Data to Analyze the Crystal's Size:

A typical XRD data is shown in FIG. 2.6. The peak broadening in the diffraction pattern is related to many factors: microstrains, faulting, crystalline domain size, and domain size distribution.[20] It is common to use the Scherrer equation to calculate the size of the crystals by using XRD data.[20] It is used to find the grain size which is less than 100 nm and this equation can be written by:

$$\boldsymbol{D = \frac{k\lambda}{W cos(\theta)}} \tag{2.5}$$

where k is a constant depends on the grain morphology and varies between 0.89 and 1.39 rad, λ is the wavelength on the incident radiation (λ= 1.542 Å), W is the full-width-at-half-maximum (FWHM), and θ is the diffraction angle.[20]

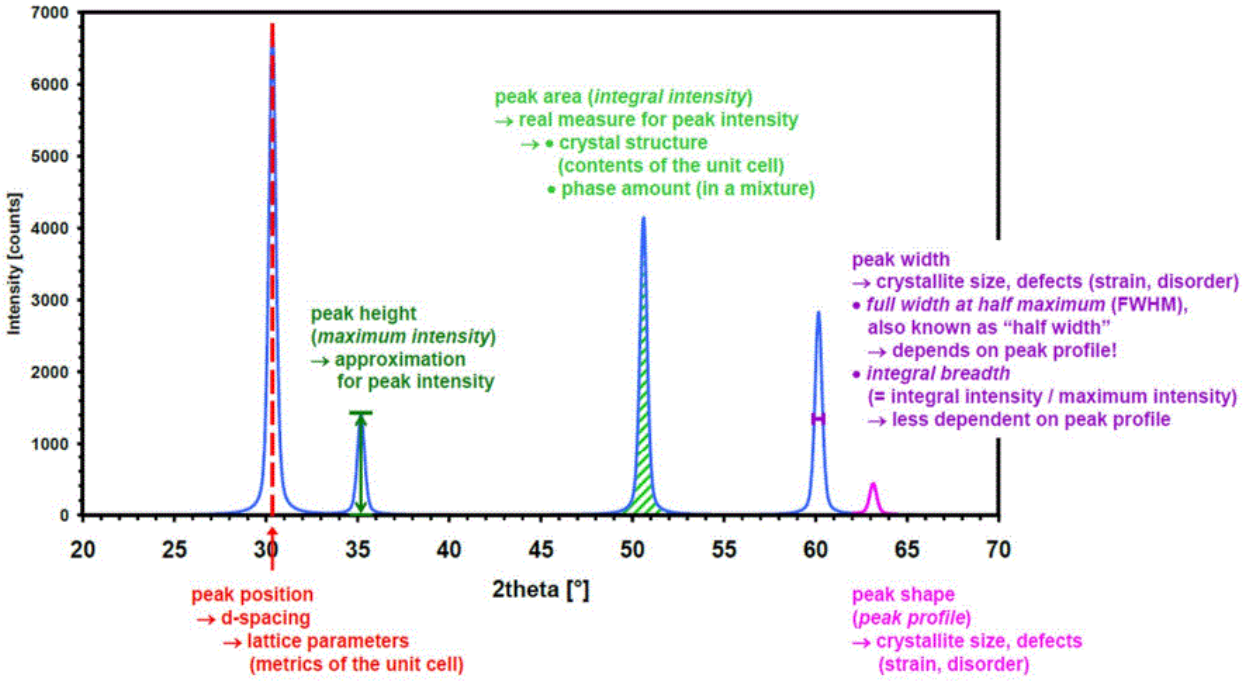

FIG. 2.6: Information content of the XRD data.[21] (Image source: http://cc.usst.edu.cn/Download/26da9cdf-6134-41fc-bf56-6dcccd9edd20.pdf)

Chapter 3: GLAD and Annealing Techniques

3.1 Glancing Angle Deposition (GLAD):

Nanoscale material fabrication can be performed in various ways, including sol-gel deposition, thermal evaporation, and sputtering.[22] GLAD is a method of deposition of gas phase atoms and molecules onto a substrate at an oblique angle. In a variation on the oblique deposition technique, the substrate is continuously moved during GLAD.[22]

The basic principle of the technique is that as an atomic flux incident on the substrate at an oblique angle, particles get deposited on nucleation sites to produce growths of tilted columns that create a series of shadowed regions in the direction of deposition flux. Due to thermal noise of growth, however, some columns grow taller than their neighbor and become dominant. This leads to "column extinction", whereby the smaller columns are eliminated completely, especially where surface diffusion is restricted at low substrate temperature $T_{substrate} \leq 0.3\ T_{melting}$, as suggested in the three zone model of Movchan and Demchishin.[23,24]

There are different basic structures formed by GLAD and can be obtained by azimuthal rotations of the substrate along two planes of incidence. Alterations along these planes let the substrate assume angles between α = (0, 90) and ϕ = (90, ∞). Column growth is controlled by defining a column and height and the corresponding orientation (α, ϕ) when the height is reached. A number of algorithms have been developed that let the user specify the height (rather than deposition time) and monitor the substrate motion accordingly.[22]

3.2 Literature Review of GLAD:

Thin film deposition and engineered nanostructure growth on substrates is a well-researched area, and numerous references to GLAD appear in literature. This review starts with the formation of regularly deposited arrays of Co and Ni on specifically patterned substrates was investigated by Dick *et al*. in 2000.[25] Clean Si or SiO_2 coated wafers were used as the substrate for growing a random film deposition. For the regular deposition process, arrays of 1000 × 1000 elements were synthesized that had a spacing of 500 nm between seed elements on the substrate. The authors found that columns had a lower diameter near the substrate followed by a larger diameter, constant diameter after the column extinction stage was reached. The same property was also observed for helices and chevrons. Some differences in magnetic properties were also observed – random deposits exhibited higher magnetic anisotropy than periodic deposits.[25]

The low temperature fabrication of periodic thin films through GLAD is of particular interest because of their low densities and highly anisotropic growth patterns. Periodicity is achieved by presenting a substrate face containing seed sites to the atom flux. A detailed analysis of this important technique, including determination of the seed size and shape, was performed by Jensen *et al*. in 2005.[26] The authors found that a circular seeding pattern was most suitable for the purpose of controlled nucleation. In addition, the seed spacing was of critical importance since the shadow cast by one seed must entirely cover the distance to its neighbor seed. In order to determine the seed spacing from center to center, *D*, they proposed the following equation for a seed height h and seed diameter d: $D = s + d \leq h \cdot tan(\alpha) + d$. The authors also observed that suppression of column growth in the interstitial spaces between seed rows is essential for achieving a well-organized structure, and they suggested that a good choice of GLAD algorithms is required for this technique.[26]

A classification of the different column growth regimes that occur after the initial nucleation phase can be found in Hawkeye *et al.* paper (2007).[24] For example, if atoms are attracted more strongly to the substrate than to each other, monolayer film deposition takes place referred to as Frank-van der Merwe growth.[24] On the other hand, greater attraction between the vapor phase atoms leads to three-dimensional island formation referred to as Volmer-Weber growth.[24] A combination of these two can also occur, with an initial monolayer growth followed by island formation. This is known as the Stranski-Krastanov growth regime.[24]

3.3 Applications of GLAD:

There are numerous applications of the GLAD technique. It is used to fabricate precisely layered 3D crystal lattices, or photonic crystals, which function as nanoscale equivalents of semiconductor crystals.[27] GLAD is especially useful in preparation of highly optically sensitive devices that exhibit large color changes with even minute differences in the ambient relative humidity (RH).[28] It has also been explored in the fabrication of pressure sensors.[28] Another promising application area of the technique is in the manufacture of nanoporous electrodes that exhibit higher power conversion efficiency when used in solar cells.[29] It has also been used for preparing large surface area Mg columns using V as a catalytic agent. These have high hydrogen storage capacities, and hence are useful as elements of fuel cells.[30]

3.4 Annealing of Metal Nanostructures

Nanostructured materials are unique in their properties and this is due to the very large percentages of atoms present at the interfaces. Their novelty can be attributed partially to quantum confinement effects also.[31] Nanostructured materials improve performance and increase capabilities of products when applied in them. They find applications in the recording, cosmetics, electric motor, tooling, automotive, duplication, aerospace, and refrigeration industries.[31]

3.5 Literature Review of Annealing of Nanostructured Materials

Nanostructured materials have a number of original and useful properties. To study these properties, annealing of several nanomaterials has been undertaken by many researchers. To begin with, Jackson and Mckenna in 1990 investigated the transition temperatures between solid and liquid phases and the heats of fusion, ΔH_f, of nonpolar organic solids.[32] These organic solids were placed in the pores of controlled porous glasses. Differential scanning calorimetry was made use of for measurements. They found that the melting point of the porous solid, $T(d)$, was lowered as pore diameter also lowered.[32]

Lewis, Jensen, and Barrat in 1997 investigated the coalescence, melting and freezing of gold nanoclusters.[33] They found that the process began first with premelting – melting of the surface, which gradually progressed inwards.[33] Wang *et al*. (1998) studied the temperature effects on the melting and shape transformations of polymer-capped cubic and tetrahedral nanocrystals.[34] They found that above temperatures of 500 °C, the particle shapes change into spheres. Above 600 °C, there is surface melting and coalescence.[34]

The annealing process of nanometer-sized decahedral Cu rods was investigated by Lisiecki *et al*. in 2000.[35] It was noticed that when the nanorods did not have any defect, they were

highly stable and the melting temperature was near the bulk phase. However, the authors found that in the presence of impurities in the nanorods, there was a dramatic decrease in the melting point.[35]

Gold nanorod changes in structure were investigated by transmission electron microcopy (TEM) by Link, Wang, and El-Sayed (2000).[36] Gold nanorods were exposed before-hand to low-energy femtosecond and nanosecond laser pulses in colloidal solution. It was discovered that the laser beams caused point and line defects in the nanorods. Thus, it was deduced that in the case of short-laser pulsed photothermal melting, it began with the induction of defects in the nanorod, which was followed by surface reconstruction and diffusion. This was found to be different from the melting of rods as in thermal melting, where there was surface melting at first.[36]

Molecular dynamics simulation was applied by Wang *et al*. (2002) to investigate the thermal stability of helical multiwall cylindrical gold nanowires.[37] It was found that the melting point of gold nanowires, which is ~ 1050 - 1100 K, seemed to be at a lower value than the bulk melting point (1375 K). However, it was at a higher value than for gold nanoclusters. The melting temperature at the interiors was also lower than the surface melting temperature in these metallic nanowires. Thus, it was concluded that the melting began from the interiors and occurred at the surface at a higher temperature.[37]

Empirical molecular dynamic simulation was applied by Wang *et al*. (2003) to study the thermal stability and melting characteristics of titanium nanowires.[38] These nanowires possessed multishell cylindrical structures. Wire size and structure determined the melting characteristics of the titanium nanowires. In thin wires of 1.2 nm, there is coexistence of solid and liquid phases. In

wires of 1.7 nm, the multishell helical structure changes to bulk-like rectangular structures. This is an important structural transformation.[38]

Karabacak *et al*. (2006) report on the melting characteristics of copper nanorod arrays.[39] These nanorods melted at temperatures much lower than the bulk melting point which was at 1083 °C. A technique called the oblique angle sputter deposition technique was utilized producing the copper nanorods. The as-deposited nanorods were 100 nm in width, 2300 nm in length and gaps of 10-30 nm separated one from the other. Various measurements such as SEM, TEM, and XRD were undertaken to study the melting process of the nanorods. It was observed that at a temperature of 400 °C, under vacuum 10^{-6} Torr, there was surface premelting. As temperatures were increased, there was coalescence in the copper nanorods and they formed a dense continuous film at 550 °C. Soldering applications may benefit from the research findings of this report.[39]

Thus, annealing of various nanowires and nanorods was carried out over the past years. The melting temperatures and characteristics were well studied in all these investigations. There are a number of applications for these research findings in industrial areas. The results of these above-mentioned works may have useful applications in low temperature soldering of materials, especially.

Chapter 4: Experiments

4.1 Sample Preparation:

Fabrication of new materials in the nanoscaled structures has an impressive effect in the nanotechnological areas. One of the capable technique which is used for that purpose is GLAD.[40] Our samples in this thesis were fabricated by using GLAD technique to create nanorod structures. In our experiments, nickel nanorod arrays were deposited by sputtering deposition on *p*-type silicon (100) with resistivity of 12 - 25 Ω cm substrates. The deposition technique was done by using the sputtering at an oblique angle which controls the direction of the incoming vapor flux to a non-normal direction under conditions of limited adatom diffusion.[39] The sample holder with the silicon substrate was rotated by a stepper motor. Thus, the large glancing angle θ of the deposition flux with respect to the substrate normal was ~ 85°. The rotation speed of the sample was controlled at 0.5 revolutions per second (rps) during the deposition. Furthermore, the distance between the vapor source and the center of the substrate was ~ 15 cm. The GLAD experiment set up is shown schematically in FIG. 4.1.

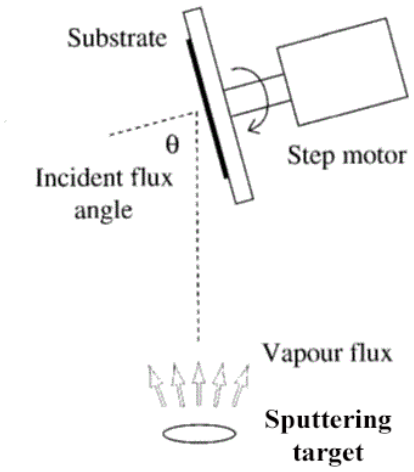

FIG. 4.1: Glancing angle deposition's technique.

Sputtering deposition is a physical vapor deposition (PVD) that involves ejecting atoms from the target onto the substrate such as a silicon wafer due to bombardment of the target by energetic ions.[41] PVD process were performed in a high vacuum chamber evacuated using a turbomolecular pump backed by a mechanical pump system with a background pressure of 2.7×10^{-8} Torr. Argon gas was injected into the chamber unit after reaching the high vacuum level in the system and it was controlled by a needle valve. During the sputter deposition process, the power was 100 watt with an ultrapure Ar pressure of 3.9 mTorr. The plasma was generated from the inert gas in the sputtering system by applying the DC high voltage on the magnetron. The magnetron in the system creates the magnetic field around the target to energize the argon ions for bombarding the target. The magnetic field restricts the electrons around the target which enhances the plasma in the chamber that increases the sputtering rate and reduces the damage to the deposited film.[42]

The adatom diffusion and atomic shadowing play the dominant role in the growth mechanism of nanorod arrays with GLAD conditions.[43] At a large tilt angle of incidence $\alpha \geq 85^{\circ}$, the initial atoms deposit on the substrate and agglomerate into microscopic clumps on the substrate. These initial stages of deposition yield shadowed regions immediately behind the clumps. The shadowing prevents the subsequent atoms from condensing in the shadowed areas. Thus, the subsequent incident flux cannot reach these areas and the atoms just deposit on the top of surface with larger heights. As the deposition continues, the arriving vapor flux has the same direction with respect to the substrate normal which caused the atoms grow into columnar structures to build the nanorods. Keeping the substrate at rest causes the resulted nanorod to align toward the vapor source. Further, by rotating the substrate unit through the sputtering, the nanorods are oriented vertically on the substrate.[44,45]

According to the kinetic energy regulation, the adatoms move on the surface diffusion during the deposition and settle in the site of lower kinetic energy producing our samples of nickel nanorods as shown in FIG. 4.2. Hence, the diffusion process is limited by the adatoms mobility or the kinetic energy of the incident atoms. By that vein, the nanorads morphology can be preserved and the individual nickel nanorod which is grown in this technique is a single crystal. Thus, the crystalline nature of nickel manufactures the nanorods tip structure.[44,45]

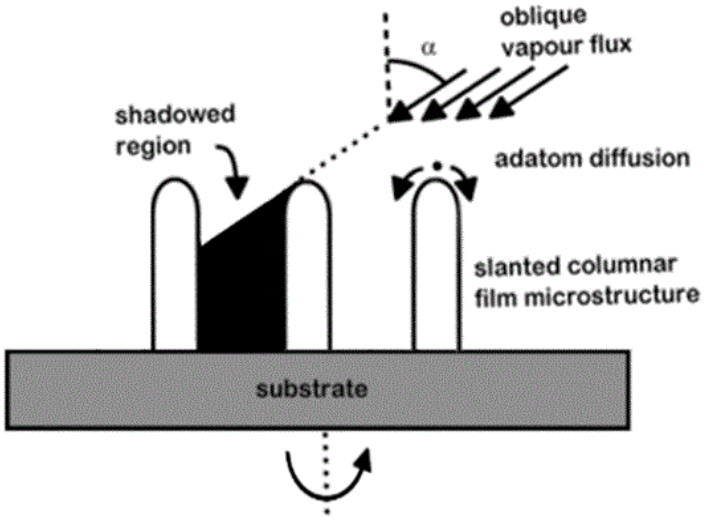

FIG. 4.2: Mechanism of nanorods growth by PVD.

In this thesis, our samples of nickel nanorod arrays were prepared at the same conditions of the deposition processes with different deposition time that controls the height of the samples. We have totally four sets of samples of 30, 50, and 90 minutes of deposition time. Furthermore, we have a thin film of 90 minutes deposition and several nickel nanorods of 90 minutes deposition for our experimental purposes of studying annealing behavior of nickel nanorods structures at various temperatures. After the deposition processes were completed, we waited the

chamber unit to cool down before removing the sample. All the samples of nickel nanorod arrays were imaged by SEM (HITACHI SU-70) to study the morphology of the samples. Furthermore, the XRD was used to study the crystalline structures of the nickel nanorod arrays.

4.2 Annealing Processes for Ni nanorods Samples:

After preparing our samples of nickel nanorod arrays, we started annealing processes to study the annealing behavior of nickel nanorods structures. Annealing processes were performed by using a split-top tube furnace to heat the nickel rods at very high temperatures. The annealing furnace can change the atomic structures and causes the metal to soften.[46] The annealing processes were done in a flow of forming gas with the pressure of about ~ 194 mTorr which was achieved using a mechanical pump. The chamber's atmosphere consists about 5% of hydrogen and 95% argon gases. The flow of the gases was adjusted to 10 sccm using a mess flow controller during the process. We studied the premelting behavior of all our samples of nickel nanorads under the condition of uniform annealing temperature at 500 °C. The premelting process was kept at 500 °C for 30 min in all our samples.

Another study in this thesis, we studied the nickel nanorod arrays within the condition of the same deposition time of 90 min deposition at different annealing temperatures which were 300 °C, 400 °C, 500 °C, and 600 °C.

The annealed Ni rods were imaged by SEM. The working distance which is the distance between the objective lens and the samples was ~ 6 mm. The accelerating voltage was varies from 5 to 10 keV. The top view and cross sectional view were taken for all our samples as shown in the next chapter.

The crystalline microstructures were studied for Ni rods by XRD using a Reflection Transmission Spinner with a Cu target operated at 45 kV and the current of 40 mA. The wave length of the Cu Kα_1 x-ray beam was 1.54 Å. The XRD θ-2θ scans were performed at an active length (2θ) of 3.347°. Our analysis of XRD data was calibrated with respect to the peak positions of the silicon (004) from the substrate. All data analysis from XRD patterns are shown in the next chapter.

Chapter 5: Experimental Results

5.1 First Study of Premelting Ni Nanorods Behaviors:

5.1.1 Crystallographic Analysis of Annealing Ni Nanorods:

As we mentioned in chapter 4, there are three sets of samples of Ni nanorods and a thin film of Ni were prepared to study annealing behavior in this thesis. XRD spectra were used to characterize the crystalline structures of all samples. XRD analysis shows the structural changes of the annealed nickel nanorod arrays. The recrystallization of the annealing process are reflected in the XRD plots of samples which demonstrate the changes in the intensity of the structural peaks as shown in this chapter from FIG. 5.1 to FIG. 5.23 for Ni (111) and Ni (200) peaks as a function of annealing temperatures. Furthermore, the peak position values acquired from XRD analysis are presented in Table 5.1.

The as-deposited Ni nanorods have a broad and weak peak of Ni (111) plane located at $2\theta \sim 44.65° \pm 0.05°$ while the peak of Ni (200) located at $2\theta \sim 54.6° \pm 0.1°$ is stronger and narrower than Ni (111) peak in almost all samples except for the sample of Ni nanorods with 30 min deposition. The Ni (200) peak is absent in that sample which indicates that the Ni nanoparticles did not grow in the (200) plane yet at that stage of deposition. When Ni nanorods grow into enough height, the growth direction switches from Ni (111) to Ni (200).

After annealing all samples at 500 °C for 30 minutes, the change of intensity was observed significantly for both peaks of Ni (111) and Ni (200). It is noted that both peaks have the huge increasing in intensity as can be seen from XRD crystallographics. Further, the XRD analysis presents similar behavior of both peaks Ni (111) and Ni (200) after annealing. It is seen that the Ni (111) peak becomes longer and stronger in intensity and narrower in width in all samples comparing with that peak before premelting. In details as demonstrated from the XRD

plots, the Ni (111) peak in the Ni nanorods with 30 min deposition was ~ 205 arb. units in intensity as-deposited and that intensity of the peak raised after annealing to be ~ 6500 arb. units. That value reflects the huge intensity change by ~ 6300 arb. units, or in another word by more than 30 times. Further, as the peak became higher, it became narrower in width by ~ 50%. However, the Ni (111) peak in the Ni nanorods with 50 min deposition grew up after annealing to reach the height of ~ 5400 arb. units where was ~ 285 arb. units height before annealing with a FWHM of 0.006 which declined after premelting the sample by ~ 38%. In addition, this peak completes to behave by that way in the Ni nanorods and Ni thin film with 90 min deposition for both to emphasize the intensity change of that peak in Ni nanorods with 90 min deposition after annealing by ~ 16400 arb. units which is less than other samples as we can see in FIG. 5.9 with a FWHM reduced by 22%. Nevertheless, the Ni thin film has a substantial intensity change in the Ni (111) peak height which was about 480 arb. units before annealing to change to ~12300 arb. units after annealing with a narrower width by about 37% than unannealed peak of Ni (111). It is noted that the Ni (111) peak of the Ni thin film with 90 min deposition is the highest peak of all the annealed samples which indicates the better crystals due to annealing process.

Moreover, the Ni (200) peak reflects the higher intensity change in all annealed samples than unannealed samples and it started to appear in the sample of Ni nanorod arrays of 30 min deposition with a height of 5400 arb. units which suggests the growth of Ni (111) grains and shift to the Ni (200) plane to be both peaks in that sample as other samples. In addition, the other samples have a dramatic change of Ni (200) peak whereas the XRD spectra present a steep rise of that peak in these samples. For instant, the Ni (200) peak increased in intensity by ~ 4600 arb. units in the nanorods samples of 90 min deposition and 50 min deposition which provide the better crystals after annealing. Further, this Ni (200) peak was about 540 arb. units height in the

as-deposited thin film of 90 min deposition that raised to about 4600 arb. units which interprets the intensity change by ~ 4000 arb. units with a reduced FWHM by ~ 22% after annealing. This reflected information of XRD spectra indicates the recrystallization and the formation of grain size changes due to annealing process. The broad and weak peak speculates the small grain size in the crystalline structure as well as in Ni (111) peak in all as-deposited samples. However, the strong and narrow satellite peak reflects the larger grain sizes of the crystalline textures. This concept leads us to expect the significant change of grain size after annealing in all samples even for the Ni thin film. Hence, the crystallographic peaks are considered to calculate the crystallite size *D* by using the Debye-Scherrer equation:

$$\boldsymbol{D = k\lambda\,/[\,W\ \cos\theta\,]} \qquad (5.\ 1)$$

where *k* is a constant depends on the particle shape and varies between 0.89 and 1.39 rad.[47] In our calculation, we used *k* = 0.9 according to many reference[47,48] which leads the Scherrer equation to be:

$$\boldsymbol{D = 0.9\,\lambda\,/[\,W\ \cos\theta\,]} \qquad (5.\ 2)$$

in which λ is the wavelength of the incident x-rays (λ = 1.542 Å), *W* is the FWHM, and θ is the half Bragg angle at the center of the peak. Table 5.2 and Table 5.3 summarize the calculated particle size (crystalline domain size *D*) of both Ni peaks (111) and (200) for all the samples before and after annealing.

It is observed from the Tables 5.2 and 5.3 that the grain size is proportional to the sample thickness that we assume the grain size of the Ni nanorods with 90 min deposition is the largest size of all the samples in both Ni (111) and Ni (200) peaks. Moreover, it is noted that the grain size increased in all samples after annealing for both Ni peaks. For instant, for Ni (111) peak, the diameter grew up after annealing by 105% in Ni nanorods (30 min deposition), 60% in Ni

nanorods (50 min deposition), 26.3% in Ni nanorods (90 min deposition), and 62% in the Ni thin film (90 min deposition). On the other hand, for Ni (200) peak, the grain size increased after annealing by 74% in Ni nanorods (50 min deposition), 41.5% in Ni nanorods (90 min deposition), and 28%in the Ni thin film with 90 min deposition. Thus, as it is noted in those two tables, the Ni (200) peak has larger grain size than Ni (111) in all as-deposited and annealed samples.

Table 5.1: The θ-2θ XRD peak positions of Ni (111) and Ni (200) for nickel nanorods and Ni thin film samples. The equilibrium 2θ values for Ni (111) and Ni (200) peaks are 44.60° and 54.60° respectively.

Samples		XRD Ni (111) 2θ peak position (^{o})	XRD Ni (200) 2θ peak position (^{o})
Ni nanorods (30 min deposition)	As-deposited	44.70 ± 0.01	N/A
	After annealing (T = 500 ^{o}C)	44.64 ± 0.01	54.68 ± 0.01
Ni nanorods (50 min deposition)	As-deposited	44.69 ± 0.01	54.73 ± 0.01
	After annealing (T = 500 ^{o}C)	44.64 ± 0.01	54.68 ± 0.01
Ni nanorods (90 min deposition)	As-deposited	44.54 ± 0.01	54.60 ± 0.01
	After annealing (T = 500 ^{o}C)	44.54 ± 0.01	54.60 ± 0.01
Ni thin film (90 min deposition)	As-deposited	44.64 ± 0.01	54.68 ± 0.01
	After annealing (T = 500 ^{o}C)	44.67 ± 0.01	54.68 ± 0.01

Table 5.2: FWHM and average grain size of Ni (111) for all samples calculated by using Scherrer equation.

Samples		FWHM	Average grain size (*D*) (nm)
Ni nanorods (30 min deposition)	As-deposited	0.0088	17
	After annealing (T = 500 ^{o}C)	0.004	35
Ni nanorods (50 min deposition)	As-deposited	0.006	25
	After annealing (T = 500 ^{o}C)	0.0037	40
Ni nanorods (90 min deposition)	As-deposited	0.0038	38
	After annealing (T = 500 ^{o}C)	0.00297	48
Ni thin film (90 min deposition)	As-deposited	0.006	24
	After annealing (T = 500 ^{o}C)	0.0038	39

Table 5.3: FWHM and average grain size of Ni (200) for all samples calculated by using Scherrer equation.

Samples		FWHM	Average grain size (*D*) (nm)
Ni nanorods (30 min deposition)	As-deposited	N/A	N/A
	After annealing (T = 500 ^{o}C)	0.0017	92
Ni nanorods (50 min deposition)	As-deposited	0.0029	54
	After annealing (T = 500 ^{o}C)	0.0017	94
Ni nanorods (90 min deposition)	As-deposited	0.0019	82
	After annealing (T = 500 ^{o}C)	0.0013	116
Ni thin film (90 min deposition)	As-deposited	0.0023	68
	After annealing (T = 500 ^{o}C)	0.0018	87

XRD spectra for Ni (111) peak in all samples

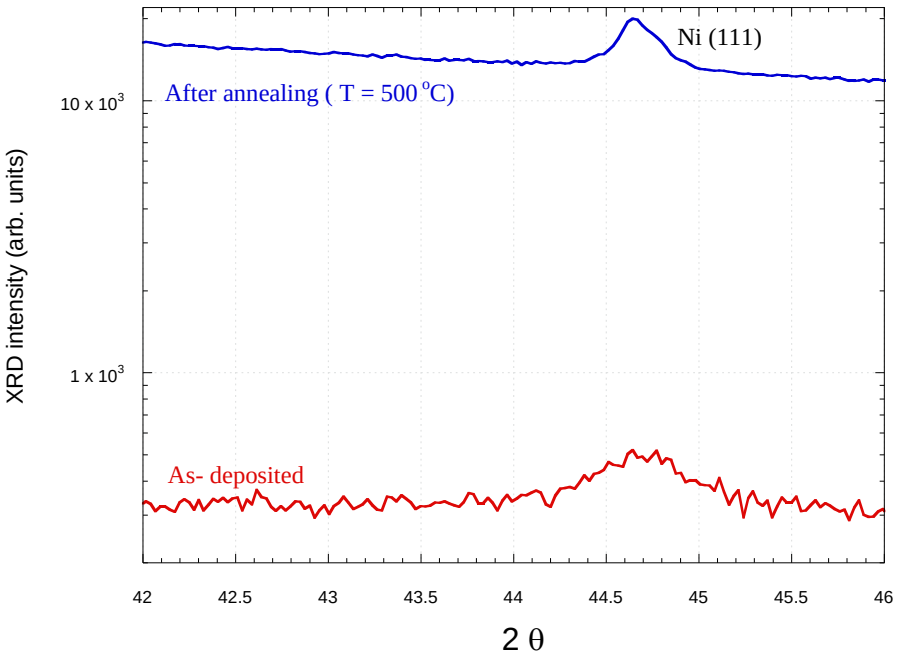

FIG. 5.1: Ni (111) peak for the Ni nanorods with 30 min deposition as-deposited and after annealing at T= 500 °C.

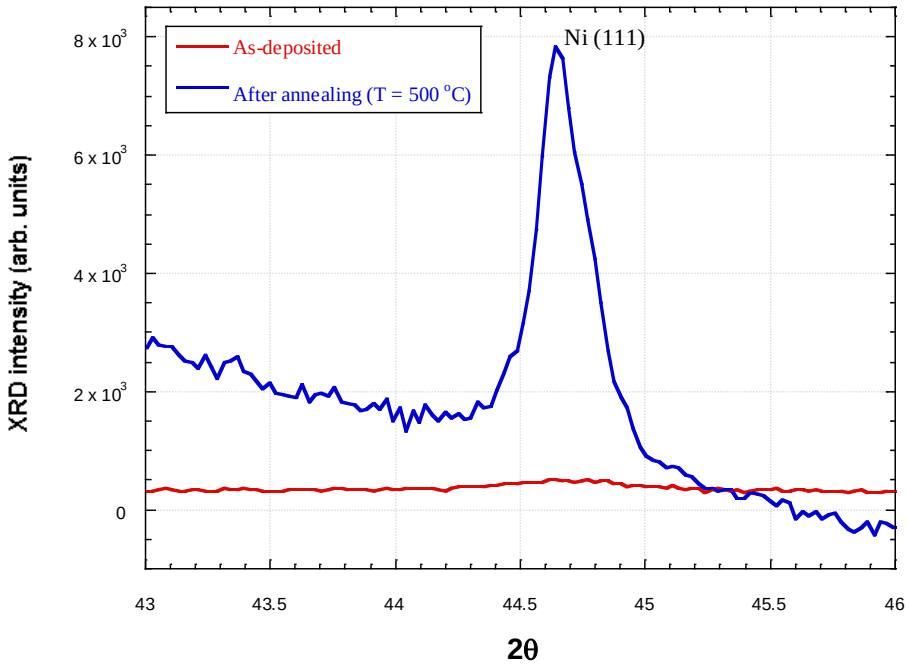

FIG. 5.2: The intensity change of Ni (111) peaks of the Ni nanorods with 30 min deposition as-deposited and after annealing at T= 500 °C.

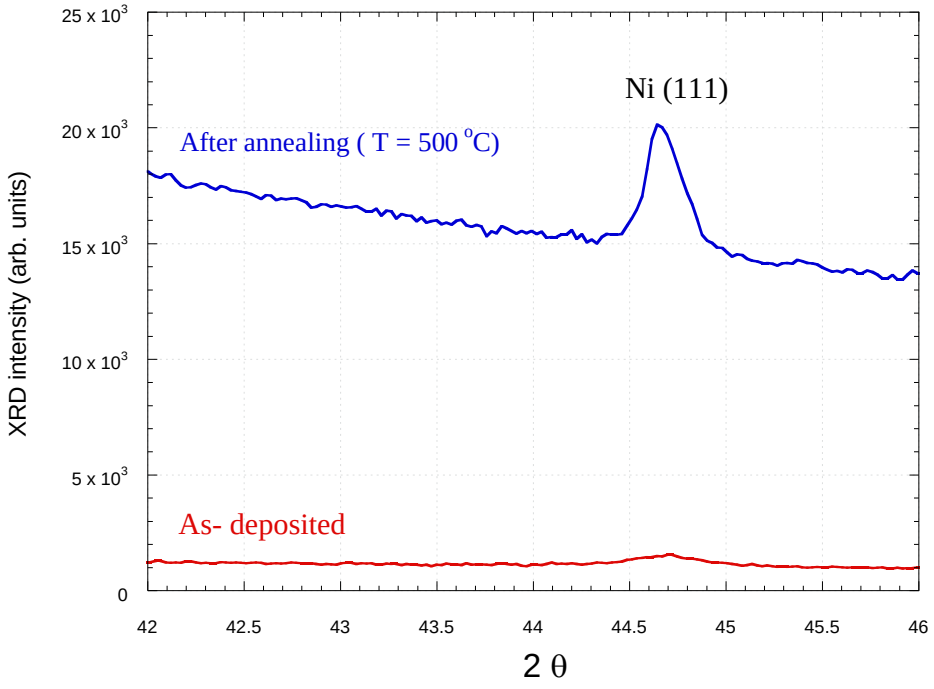

FIG. 5.3: Ni (111) peak for the Ni nanorods with 50 min deposition as-deposited and after annealing at T= 500 °C.

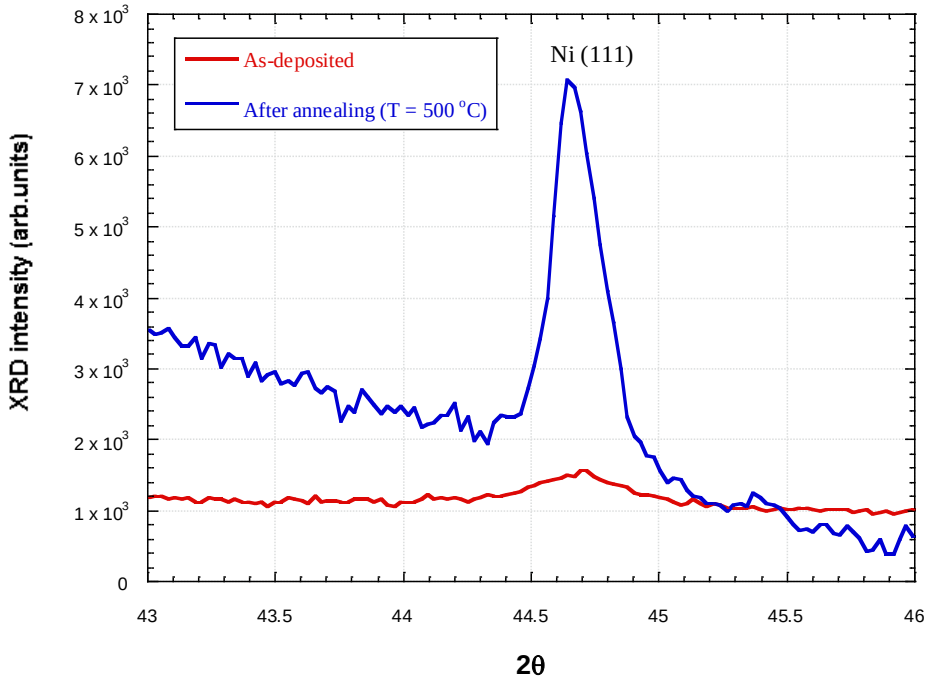

FIG. 5.4: The intensity change of Ni (111) peaks of the Ni nanorods with 50 min deposition as- deposited and after annealing at T= 500 °C.

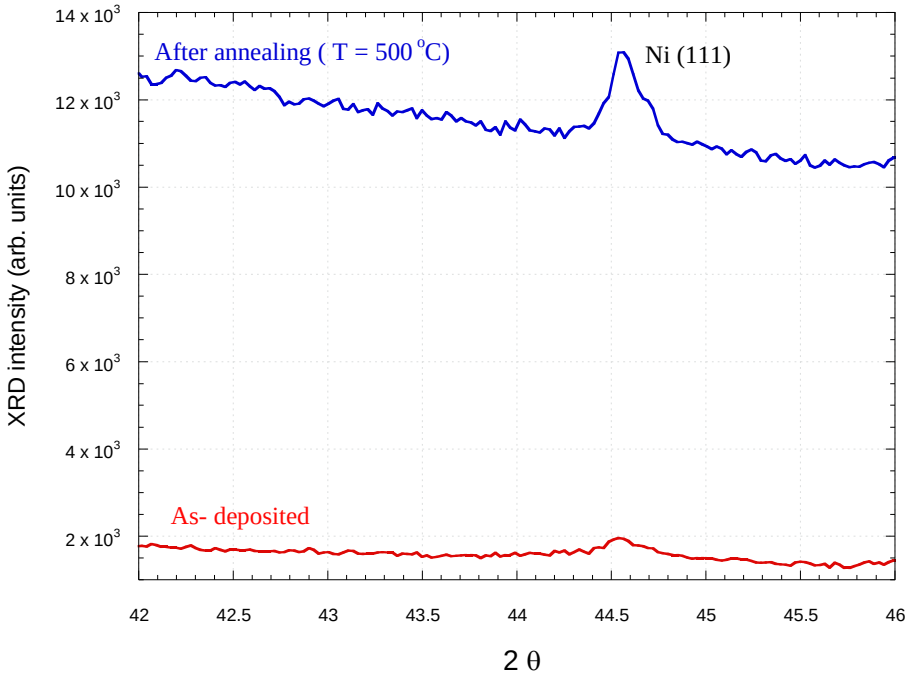

FIG. 5.5: Ni (111) peak for the Ni nanorods with 90 min deposition as-deposited and after annealing at T= 500 °C.

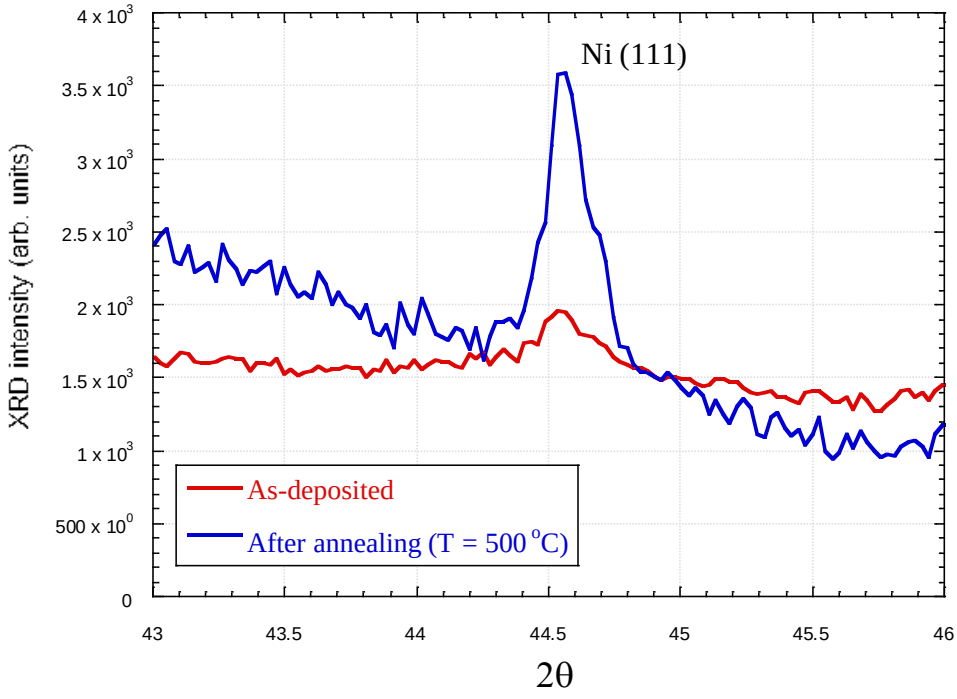

FIG. 5.6: The intensity change of Ni (111) peaks of the Ni nanorods with 90 min deposition as-deposited and after annealing at T= 500 °C.

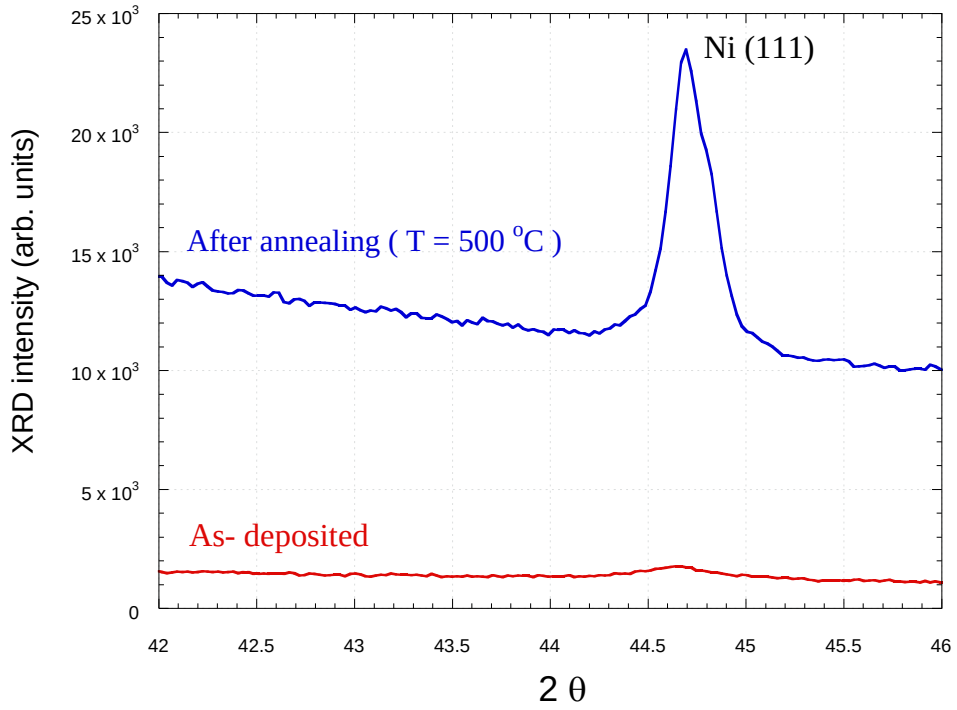

FIG. 5.7: Ni (111) peak for the Ni thin film with 90 min deposition as-deposited and after annealing at T= 500 °C.

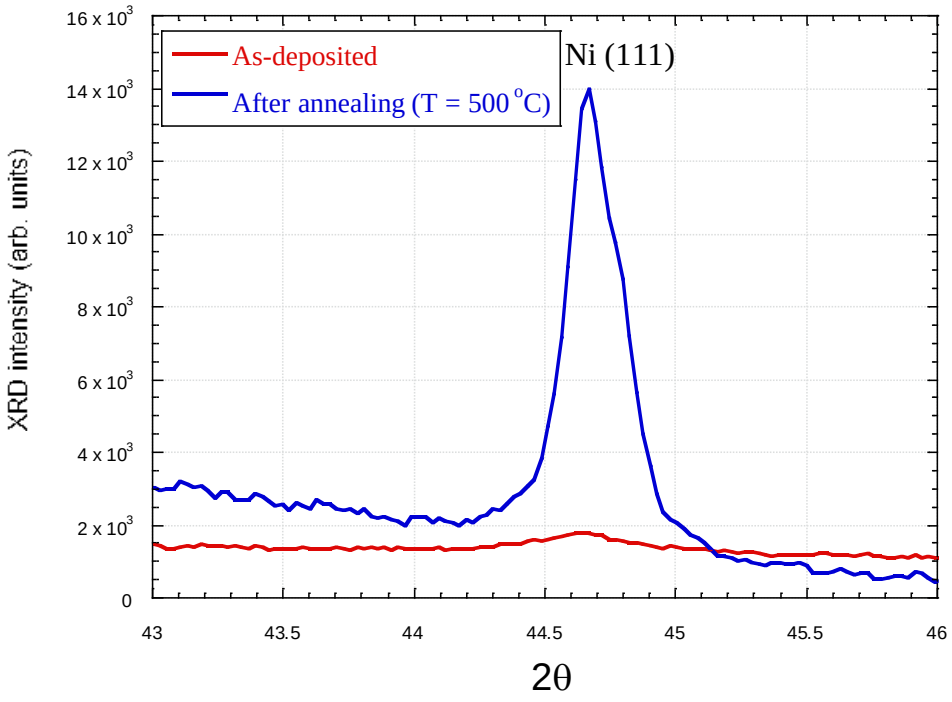

FIG. 5.8: The intensity change of Ni (111) peaks of the Ni thin film with 90 min deposition as-deposited and after annealing at T= 500 °C.

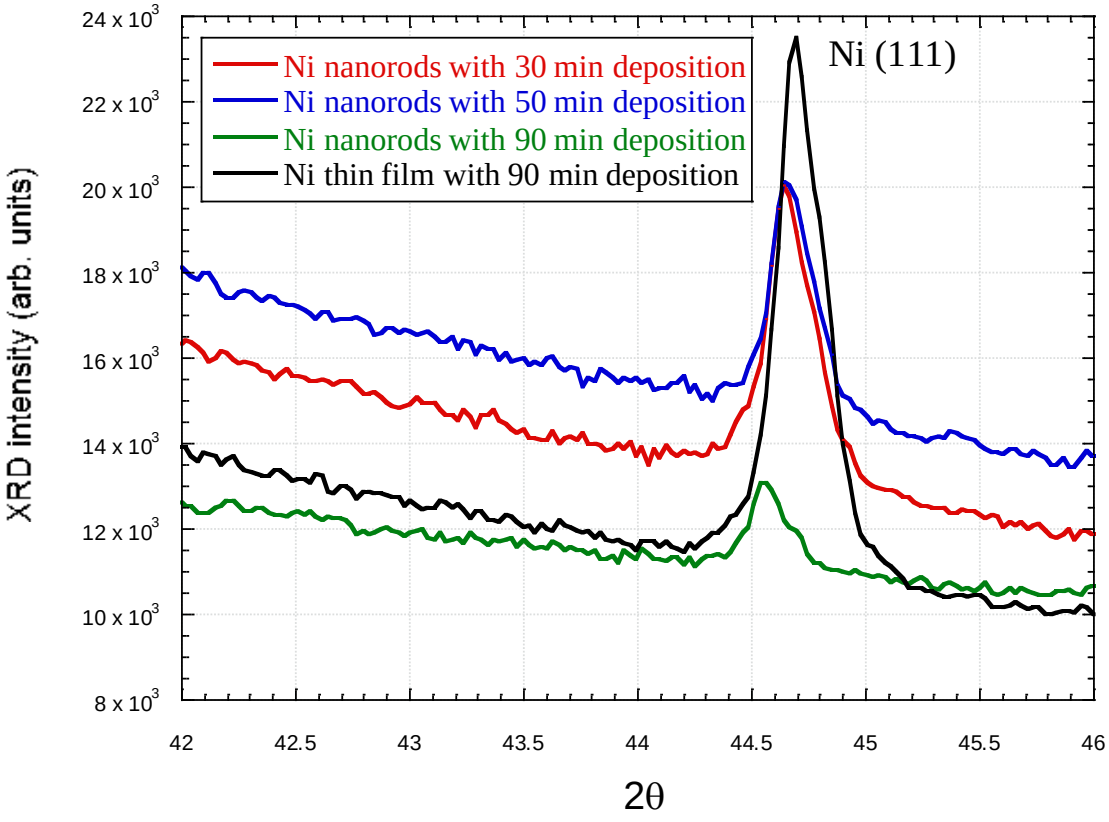

FIG. 5.9: The comparison of Ni (111) peak for all the samples after annealing at T= 500 ^{o}C.

XRD spectra for Ni (200) peak in all samples

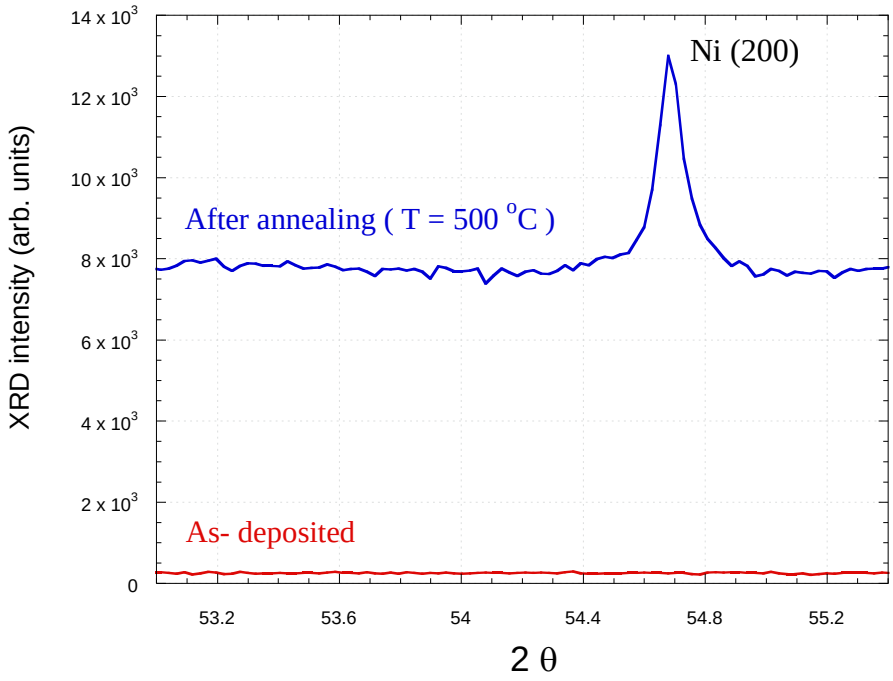

FIG. 5.10: Ni (200) peak for the Ni nanorods with 30 min deposition as-deposited and after annealing at T= 500 °C.

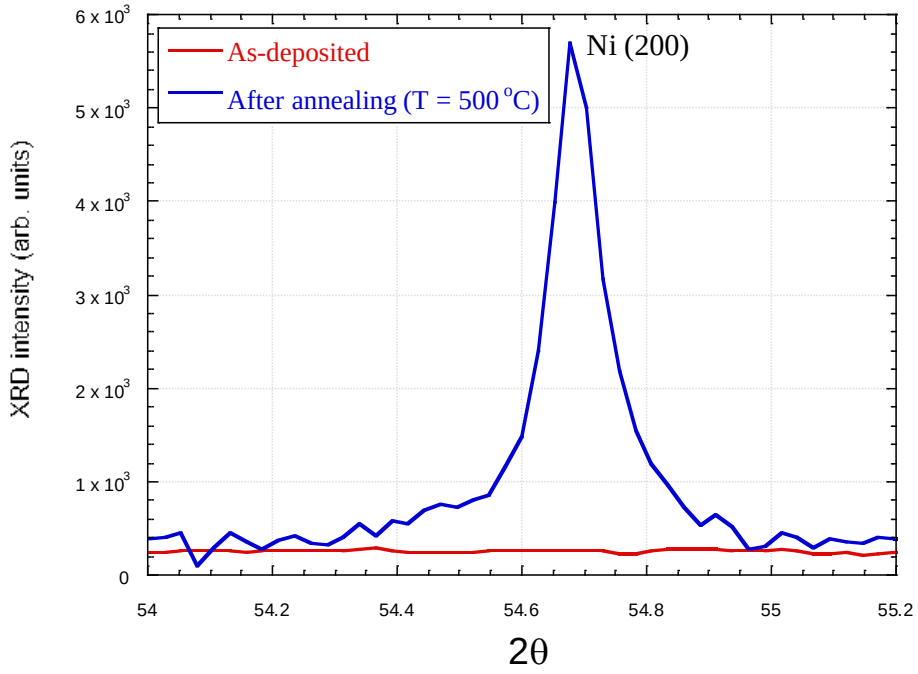

FIG. 5.11: The intensity change of Ni (200) peak of the Ni nanorods with 30 min deposition as- deposited and after annealing at T= 500 °C.

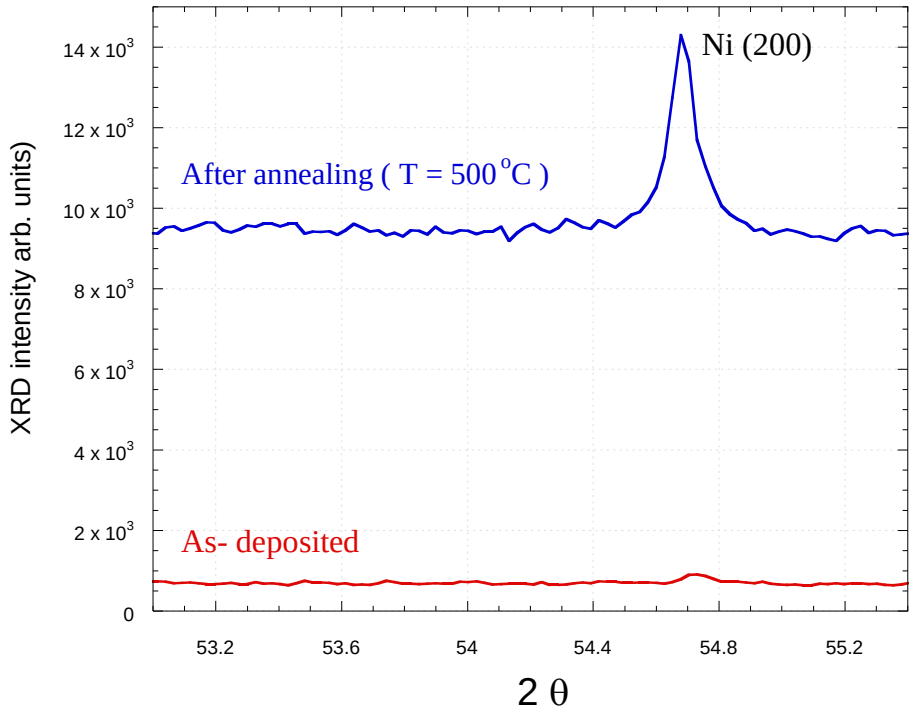

FIG. 5.12: Ni (200) peak for the Ni nanorods with 50 min deposition as-deposited and after annealing at T= 500 °C.

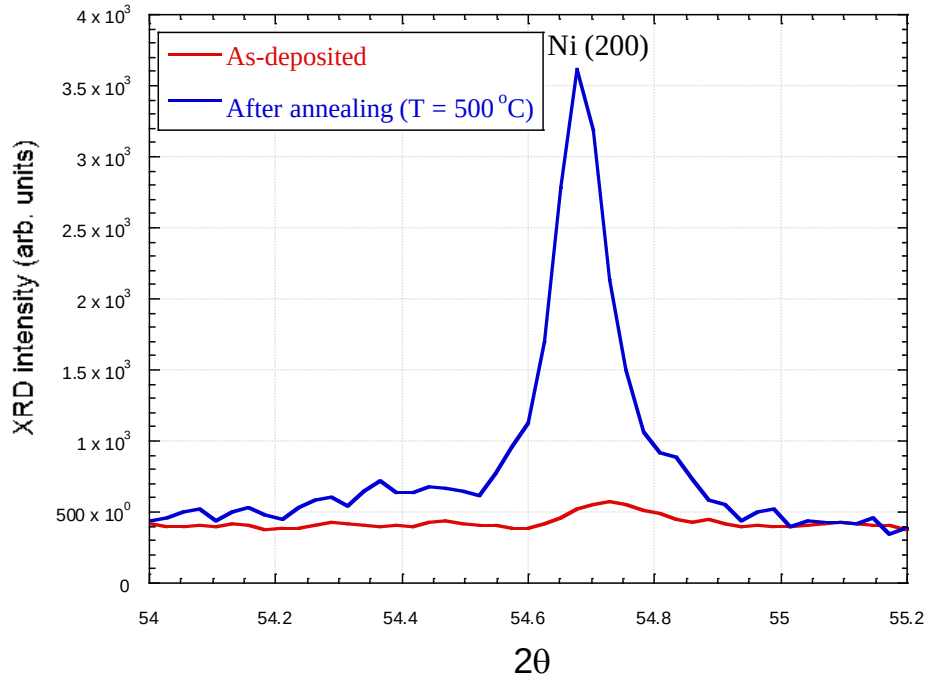

FIG. 5.13: The intensity change of Ni (200) peak of the Ni nanorods with 50 min deposition as-deposited and after annealing at T= 500 °C.

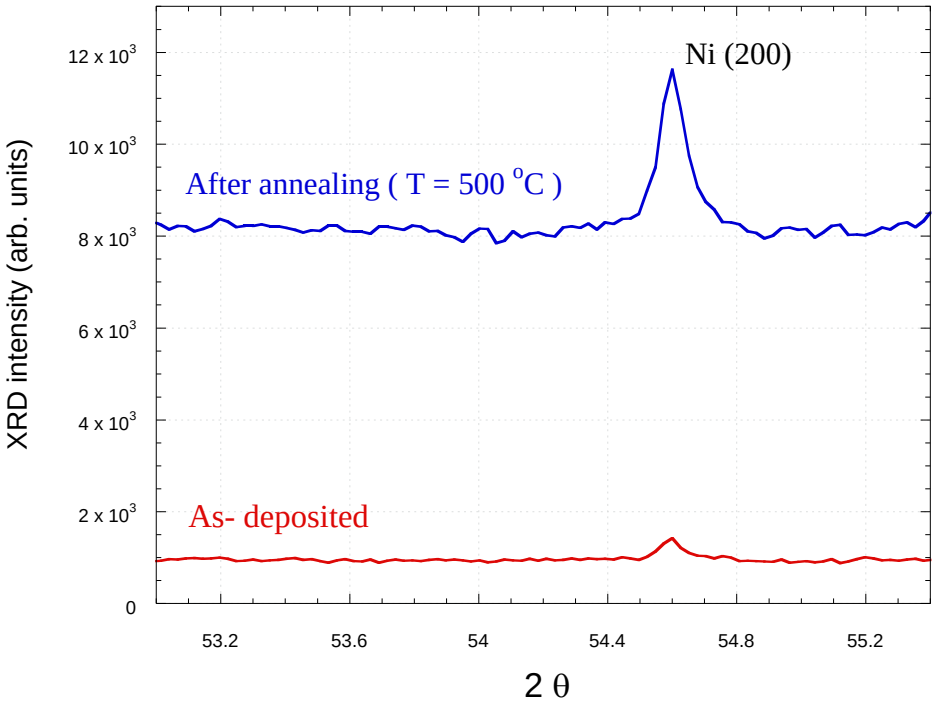

FIG. 5.14: Ni (200) peak for the Ni nanorods with 90 min deposition as-deposited and after annealing at T= 500 °C.

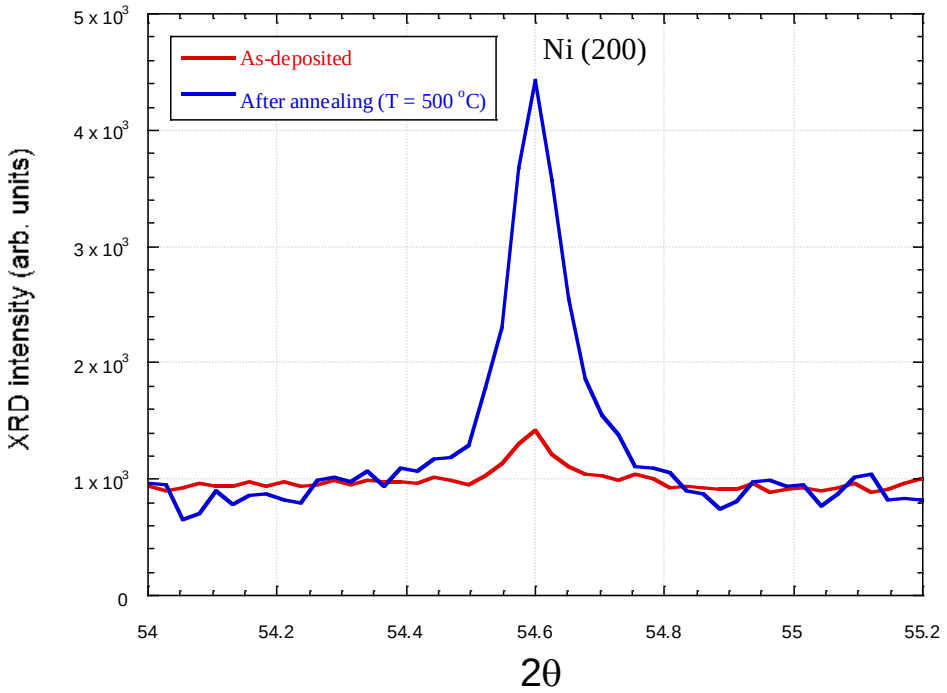

FIG. 5.15: The intensity change of Ni (111) peak of the Ni nanorods with 90 min deposition as-deposited and after annealing at T= 500 °C.

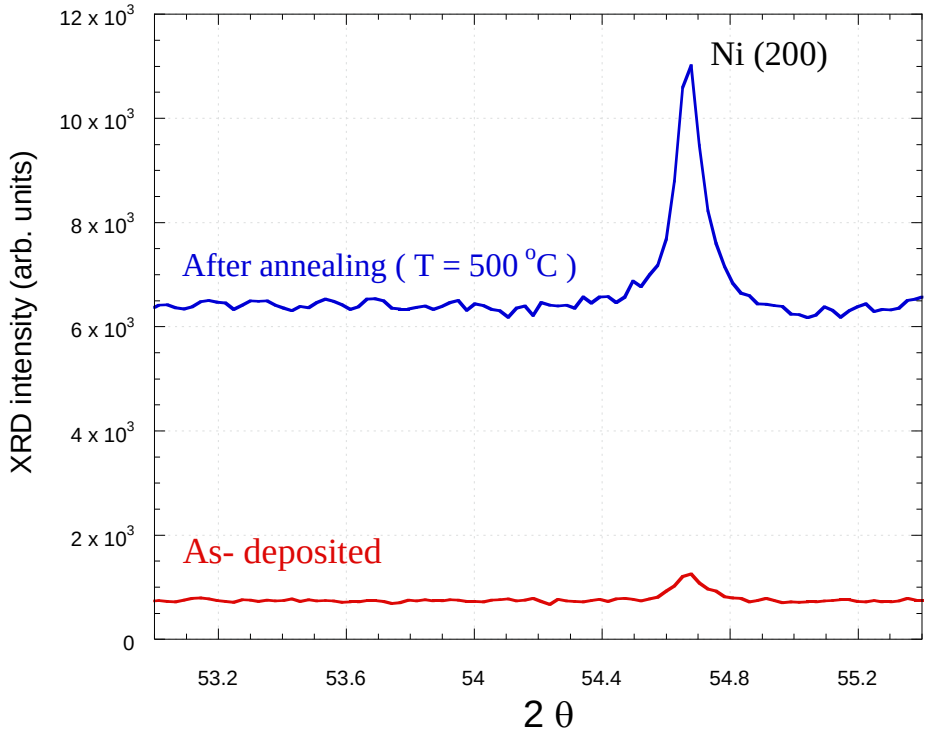

FIG. 5.16: Ni (200) peak for the Ni thin film with 90 min deposition as-deposited and after annealing at T= 500 °C.

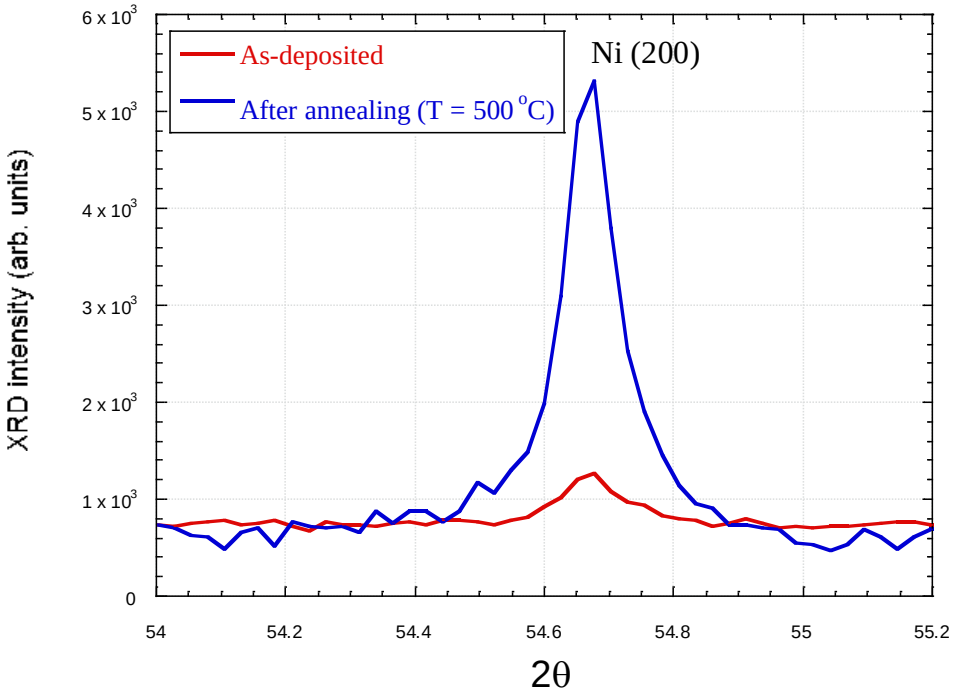

FIG. 5.17: The intensity change of Ni (200) peak of the Ni thin film with 90 min deposition as-deposited and after annealing at T= 500 °C.

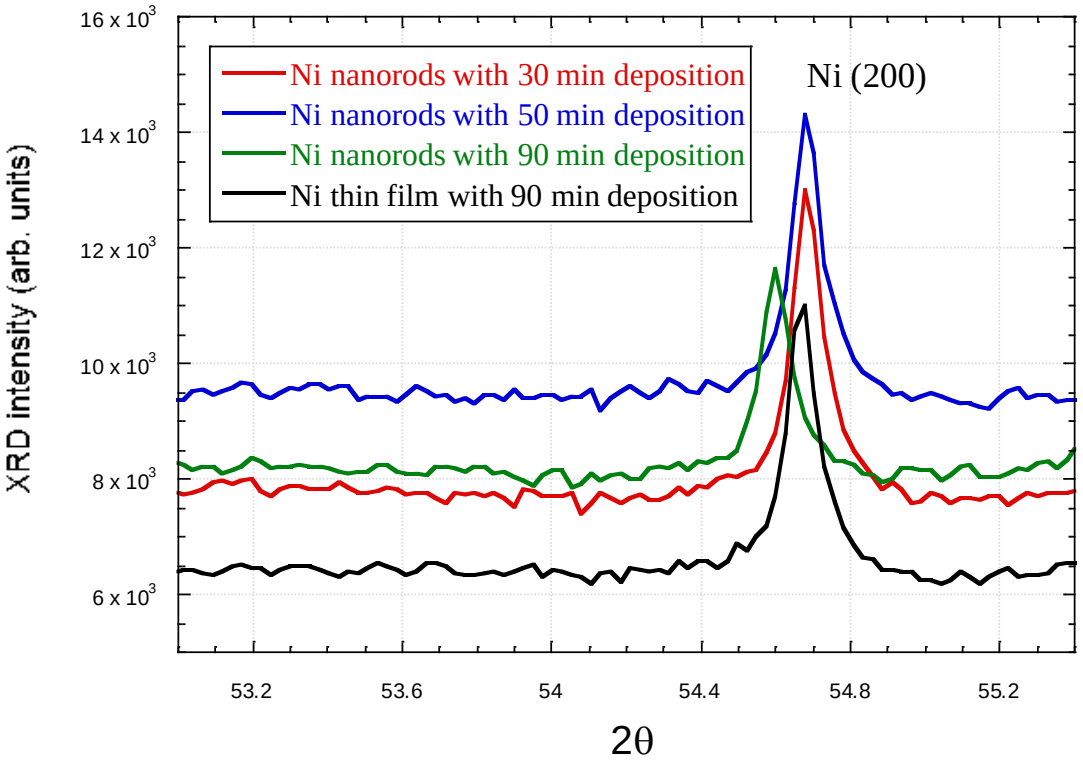

FIG. 5.18: The comparison of Ni (200) peak for all the samples after annealing at T= 500 ^{o}C.

XRD spectra for both Ni (111) and Ni (200) peaks in all samples

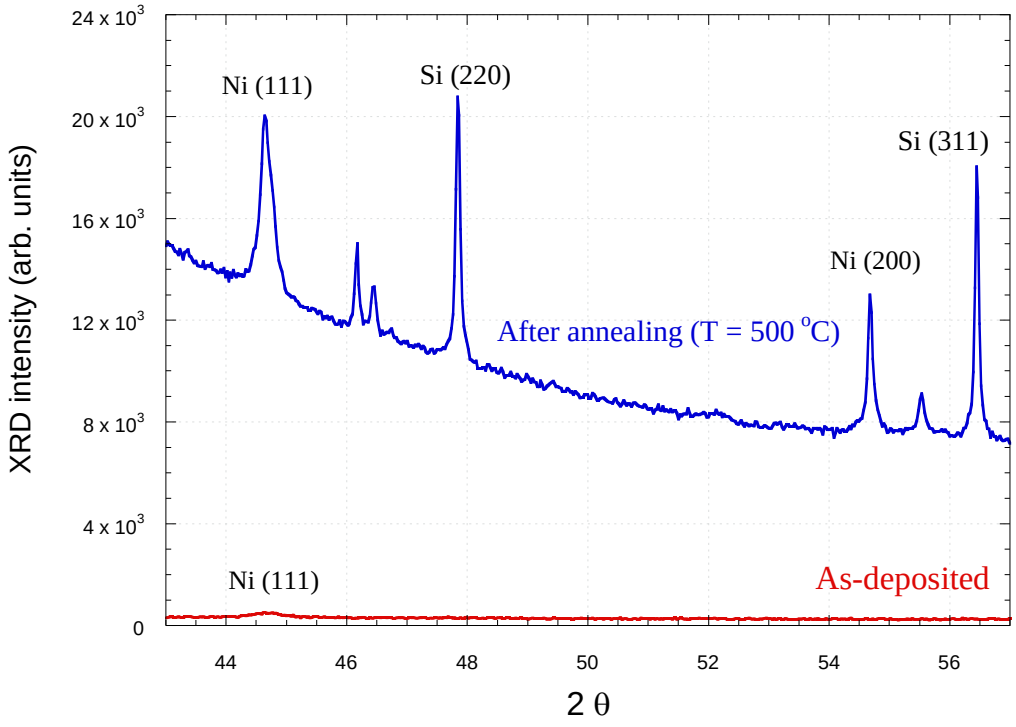

FIG. 5.19: Both Ni peaks in the Ni nanorods with 30 min deposition as-deposited and after annealing at T = 500 °C.

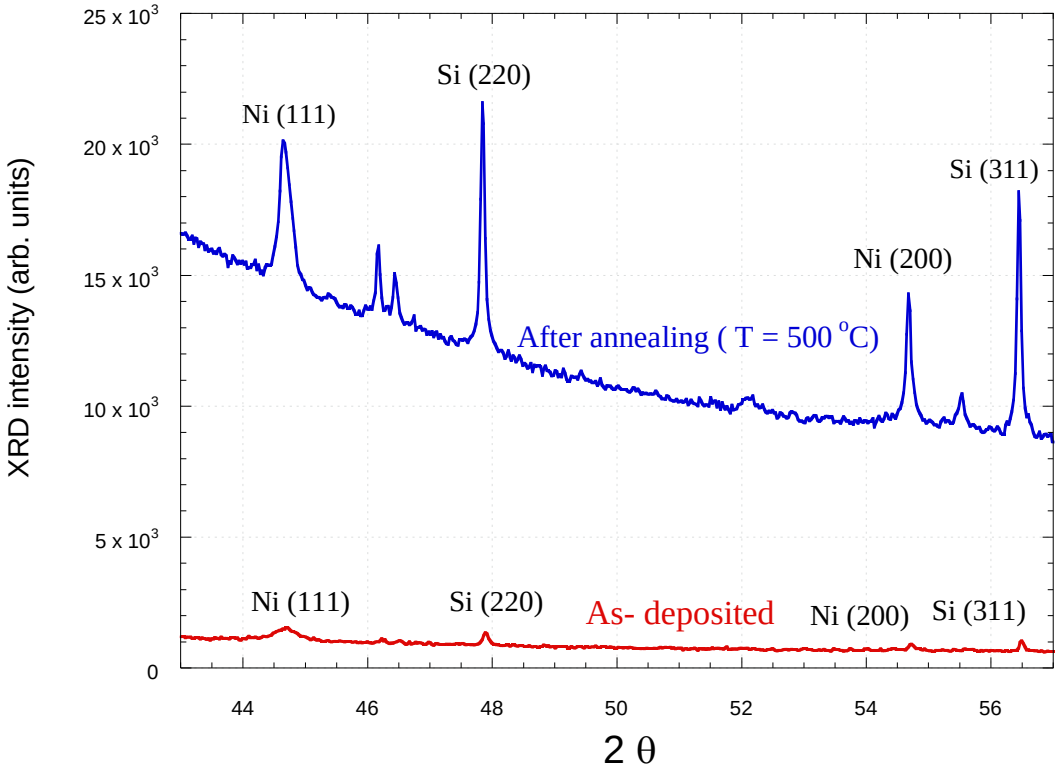

FIG. 5.20: Both Ni peaks in the Ni nanorods with 50 min deposition as-deposited and after annealing at T = 500 °C.

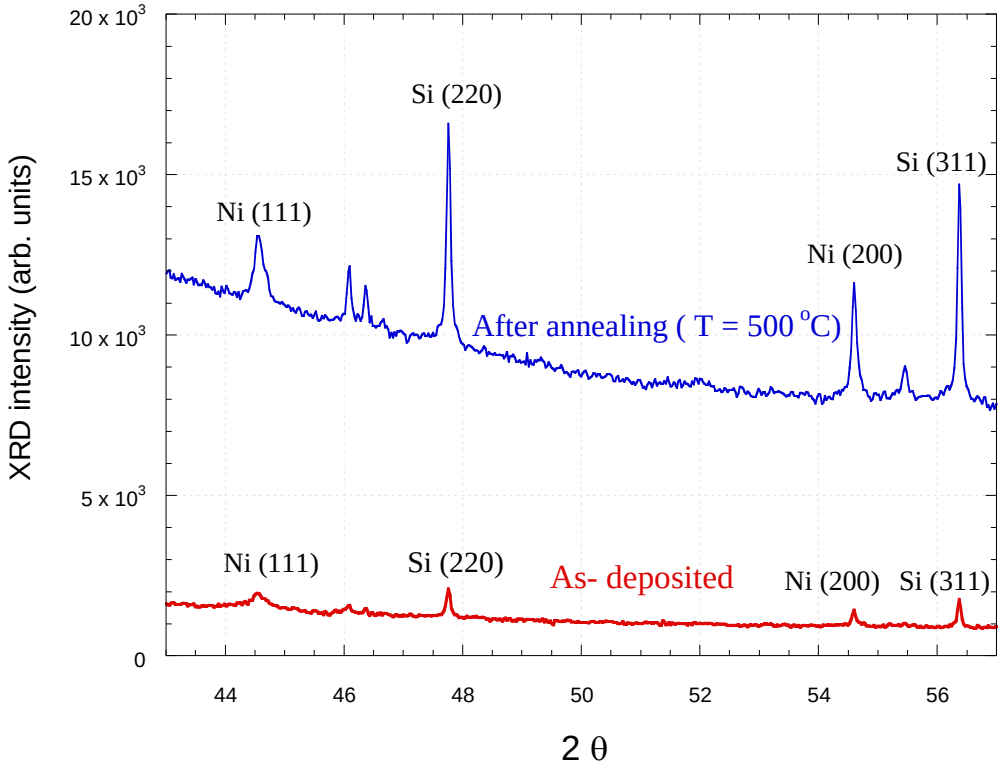

FIG. 5.21: Both Ni peaks in the Ni nanorods with 90 min deposition as-deposited and after annealing at T = 500 °C.

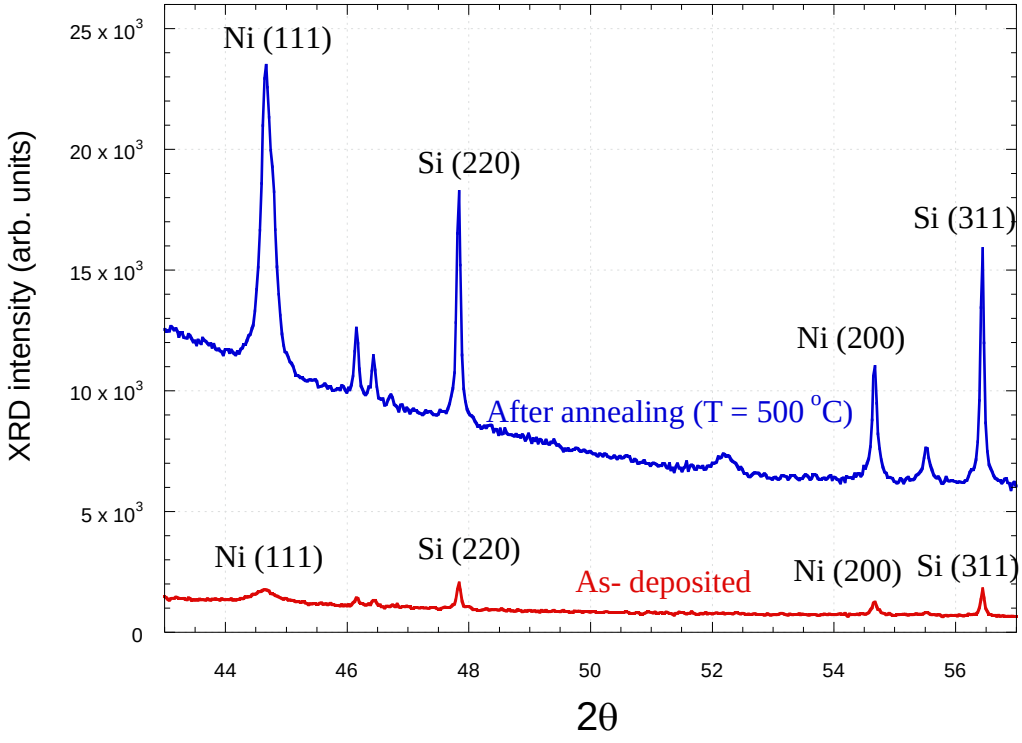

FIG. 5.22: Both Ni peaks in the Ni thin film with 90 min deposition as-deposited and after annealing at T = 500 °C.

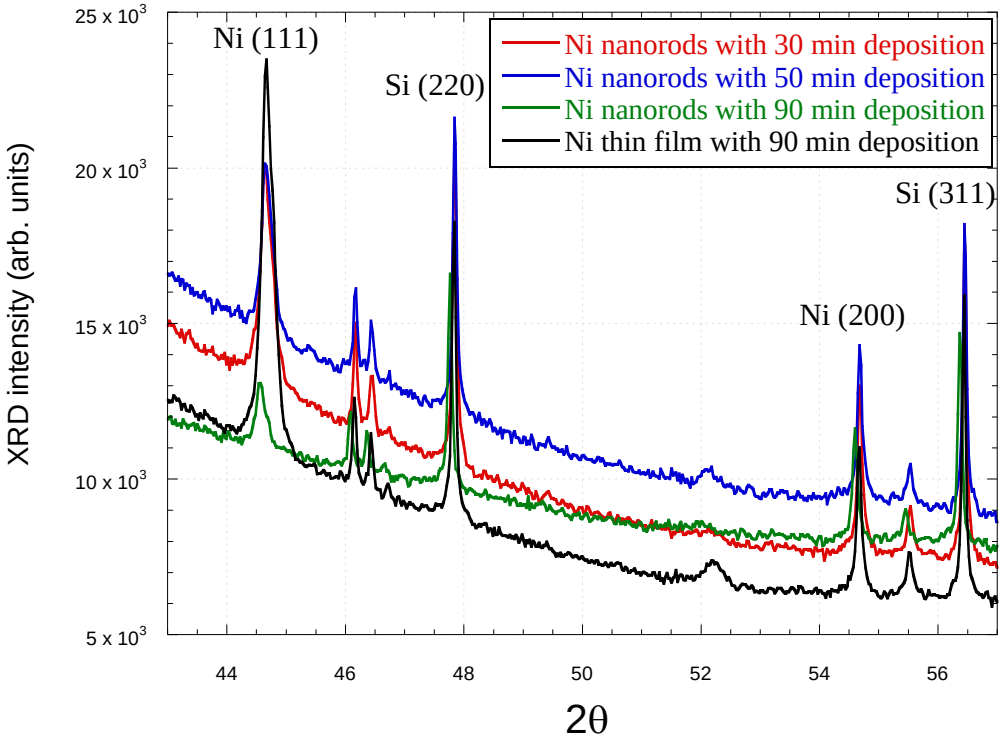

FIG. 5.23: The comparison of both Ni peaks in all the samples after annealing at T = 500 °C.

5.1.2 Morphological Changes of Ni nanorod Arrays Due to Annealing Process:

Figures 5.24, 5.25, 5.26, and figure 5.27 show the top view and cross-sectional view SEM images of as-deposited Ni nanorods and annealing effects on different Ni nanorods samples. The morphological changes of Ni nanorod arrays are clearly observed after annealing samples in this study at T = 500 °C. As can be seen the rods are grown vertically on the silicon substrate by using GLAD. The columns of the Ni nanorods are deposited on the substrate and separated from each other with gaps due to the shadowing effect regions. The shape of Ni nanorods looks like the pentagonal prism with a pyramidal tip as can be seen in SEM images and it has this form due to the crystalline nature of nickel which assumed to be face centered cubic. Further, it is observed that the thicknesses and diameters of the nickel nanorods are proportional to the deposition time which assumed that the Ni nanorods of 90 min deposition has the largest diameter and thickness of all samples. It is noted also that the Ni thin film does not have the pyramidal tip as well as nanorods does and this tip appears clearly as the columns grow up by increasing the time of deposition as can be obvious in the cross-sectional SEM image of the as-deposited Ni nanorods with 90 min deposition in FIG. 5.27

After annealing the samples with different thicknesses at T = 500 °C, the remarkable change of the nanorods morphology was observed. The rods appear to merge to each other and start to loss their edges to seem that have cylindrical shapes without pyramidal apexes as can be seen in SEM images. The columns coalesce and deform in a structural densification correlated with the rods collapse and tilting gradually towards the substrate surface. As a result of rods deformation, the pores originate from the gaps between the Ni nanorods. Furthermore, it is realized that the thickness of the nanorods decreased after annealing due to the columns collapse to each other. As displayed in the Table 5.4, the height of all samples declined after annealing

such as the height of Ni nanorods decreased by ~ 26% in the sample of 30 min deposition and by 35.7% in the sample of 50 min deposition. However, that height reduced by 30 nm in the sample of 90 min deposition where was ~ 550 nm heights before annealing and became ~ 520 nm heights after annealing shrinking by 5.4% only. Yet, the height of Ni thin film was ~ 133 nm before premelting and decreased to be ~ 120 nm after shrinking by about 10%. All these features of the nanorods deformation can be seen in the cross-sectional SEM images. All the morphological changes of the Ni nanorod arrays indicate the grain size change within premelting process. It is suggested that the grain size increases after annealing Ni nanorods at T = 500 °C due to the expansion of the paricles with increasing temperature which yeilds the rods to fuse together. As can be measured from SEM images, the diameter of the Ni rods rose from ~ 35 to ~ 75 nm in the Ni nanorods with 30 min deposition and doubled in the sample of 50 min deposition. Moreover, it also doubled in the sample of 90 min deposition after annealing to reach ~ 157 nm where was ~ 84 nm before. By the same vein, the grain size of the Ni thin film also raised to around 52 nm after annealing. The as-deposited nanorods heights and diameters were measured from SEM images and they are summarized in Table 5.4. It is observed that the measured values of heights and diameters obtained from SEM images for all as-deposited samples are reasonable and in agreement with our calculation of particle diameter by Scherrer equation on XRD peaks. These results lead us to the second study of annealing nickel nanorod arrays to compare the premelting behavior of varies annealing temperatures.

Table 5.4: The diameter (*D*) and the height of all as-deposited and annealed samples at T= 500 °C as measured from SEM images.

Samples		Average grain size (*D*) (nm)	Height (*h*) (nm)
Ni nanorods (30 min deposition)	As-deposited	35 ± 10	135 ± 2
	After annealing (T = 500 ^{o}C)	75 ± 10	100 ± 5
Ni nanorods (50 min deposition)	As-deposited	52 ± 10	350 ± 10
	After annealing (T = 500 ^{o}C)	142 ± 20	225 ± 10
Ni nanorods (90 min deposition)	As-deposited	84 ± 10	550 ± 10
	After annealing (T = 500 ^{o}C)	157 ± 10	520 ± 10
Ni thin film (90 min deposition)	As-deposited	40 ± 10	133 ± 2
	After annealing (T = 500 ^{o}C)	52 ± 5	120 ± 5

SEM images of all the samples

Ni nanorods with 30 min deposition

As-deposited sample

Top view

Cross-section

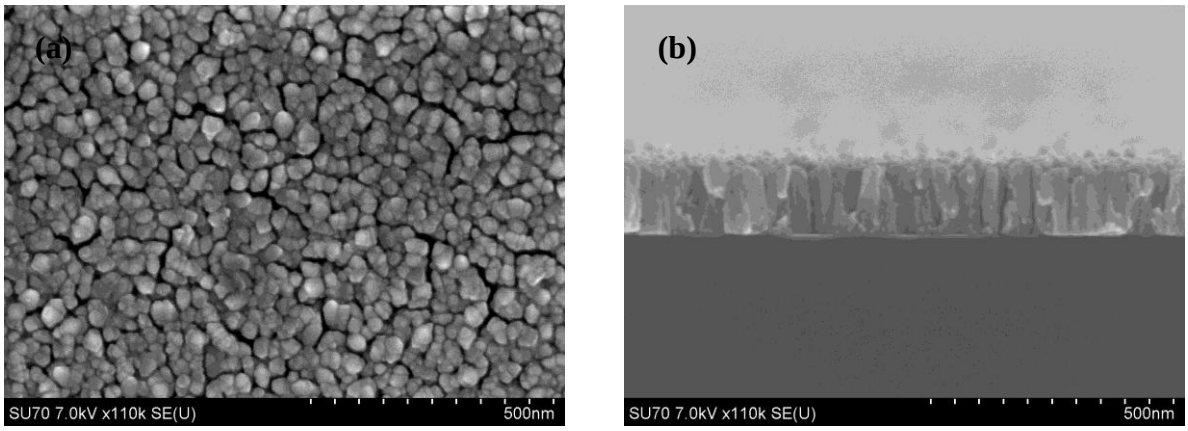

Annealed Sample at T = 500 °C

Top view

Cross-section

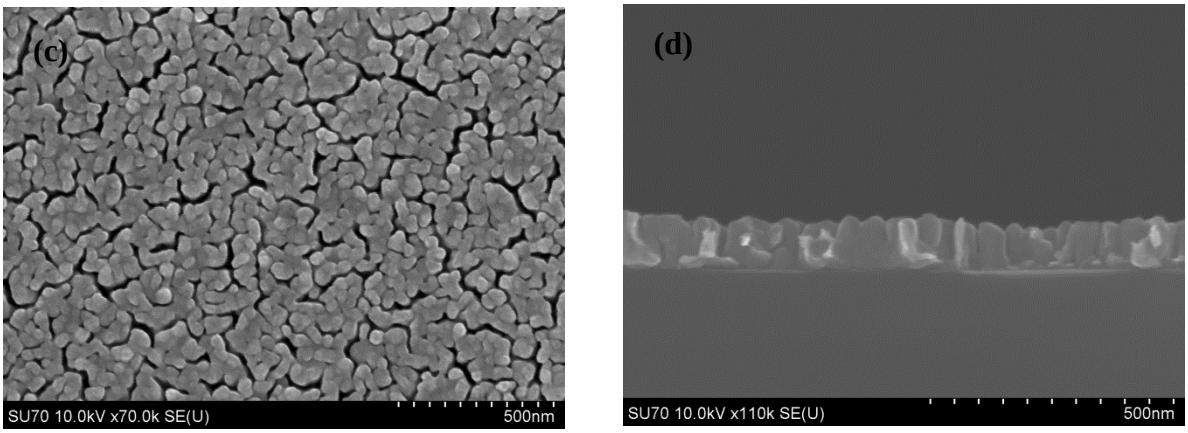

FIG. 5.24: SEM images of Ni nanorods sample (30 min deposition). (a) and (b) are the top view and cross- sectional view of as-deposited sample respectively, (c) and (d) are the top view and cross- sectional view of annealed sample at T = 500 °C respectively.

Ni nanorods with 50 min deposition

As-deposited sample

Top view

Cross-section

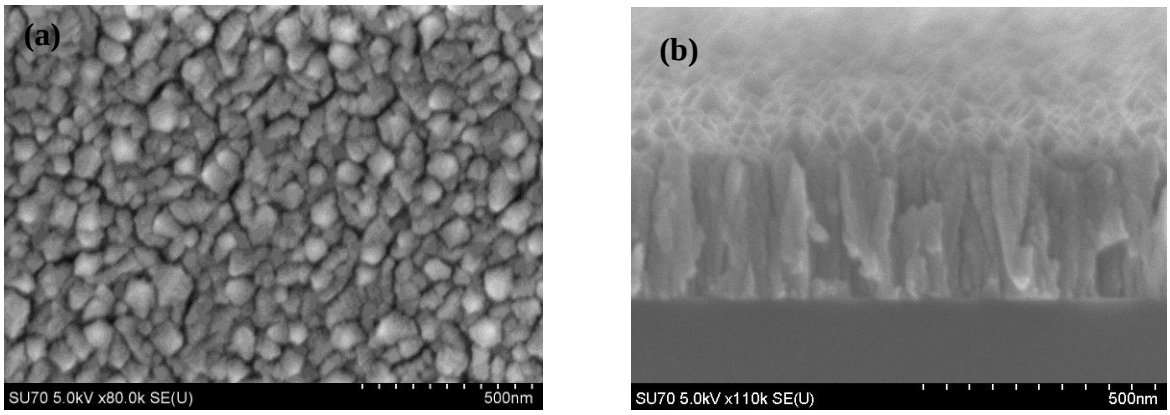

Annealed Sample at T = 500 °C

Top view

Cross-section

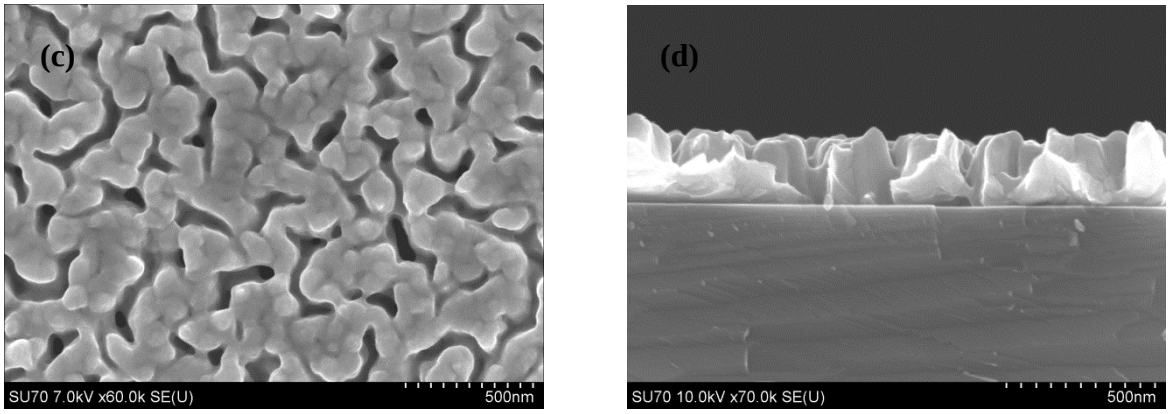

FIG. 5.25: SEM images of Ni nanorods sample (50 min deposition). (a) and (b) are the top view and cross-sectional view of as-deposited sample respectively, (c) and (d) are the top view and cross-sectional view of annealed sample at T = 500 °C respectively.

Ni nanorods with 90 min deposition

As-deposited sample

Top view

Cross-section

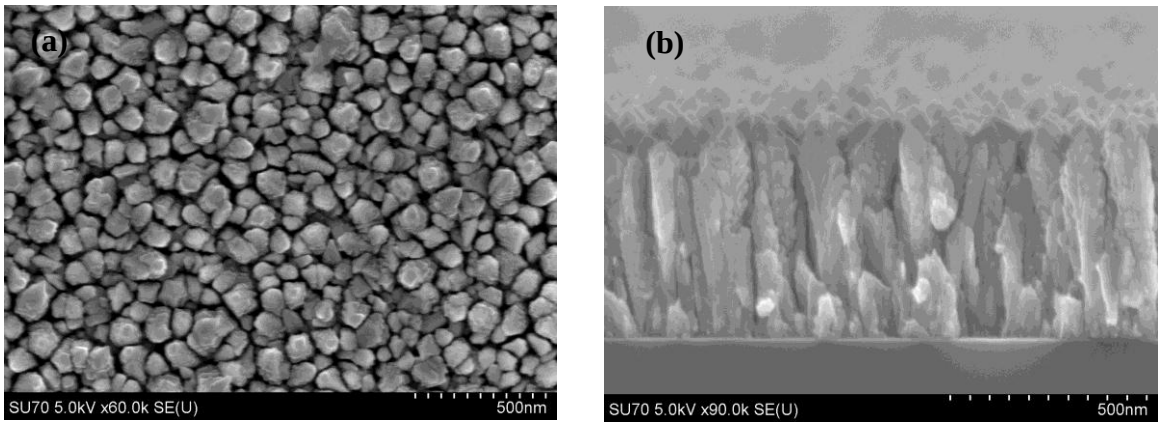

Annealed Sample at T = 500 °C

Top view

Cross-section

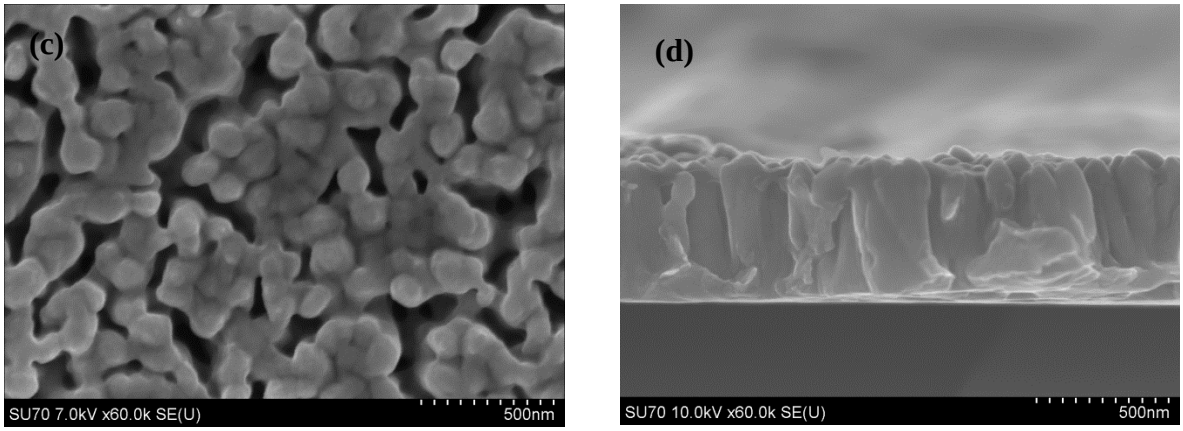

FIG. 5.26: SEM images of Ni nanorods sample (90 min deposition). (a) and (b) are the top view and cross-sectional view of as-deposited sample respectively, (c) and (d) are the top view and cross-sectional view of annealed sample at T = 500 °C respectively.

Ni thin film with 90 min deposition

As-deposited sample

Top view

Cross-section

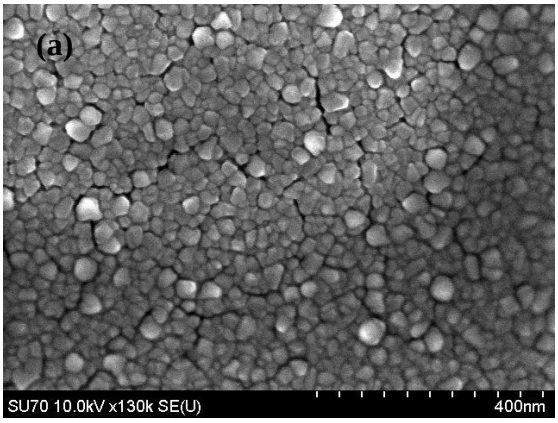

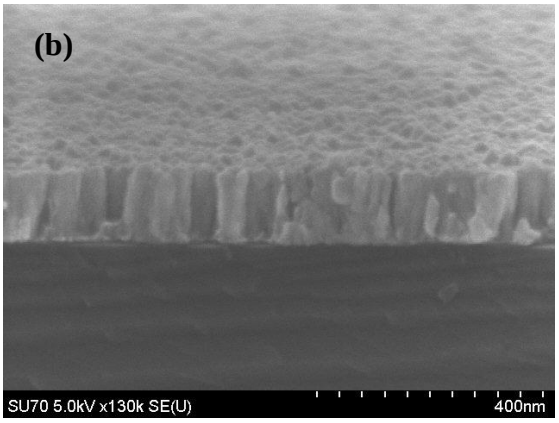

Annealed Sample at T = 500 °C

Top view

Cross-section

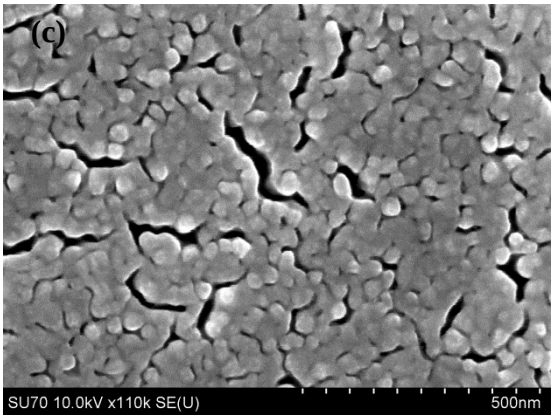

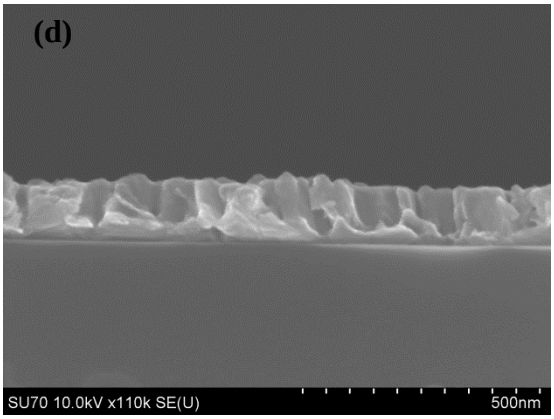

FIG. 5.27: SEM images of Ni thin film sample (90 min deposition). (a) and (b) are the top view and cross-sectional view of as-deposited sample respectively, (c) and (d) are the top view and cross-sectional view of annealed sample at T = 500 °C respectively.

5.2 The Temperature Dependent of Premelting Ni nanorods Behaviors:

5.2.1 : Crystallographic Analysis of Temperature Dependent of Annealing Ni nanorod Arrays:

In this section of this thesis, three samples of Ni nanorod arrays with 90 min deposition were annealed in the same conditions of experimental set up but each one at a different temperature which were 300 °C, 400 °C, and 600 °C. The results were characterized by using XRD spectra and compared also with the previous results of annealing that sample at 500 °C. As measured before, the as-deposited Ni nanorods have a weak peak of Ni (111) at the peak position of 2θ ~ 44.54° which is ~ 1250 arb. units in intensity with a full width at half maximum of ~ 0.004. The other peak of Ni is located at 2θ ~ 54.59° in (200) orientation and it is around 1450 arb. units in intensity which indicate that this peak is stronger than Ni (111) peak. These different intensities provide different diameters were measured by using the Scherrer equation to be ~ 36.5 nm for Ni (111) direction and ~ 82 nm for Ni (200) peak.

Starting annealing the sample at 300 °C, the trivial change in the crystallization of the Ni (111) is noted. The peak intensity changed to be 1950 arb. units with FWHM reduced by ~ 5% than as-deposited one. Further, the diameter of the nanorods increased slightly by ~ 5.6 % than before. However, this intensity change increases as the temperature is increased gradually. It is observed that the intensity of Ni (111) rose trivially after annealing at 400 °C to increase the diameter of Ni nanorods by ~ 20% than the previous temperature where was ~ 38.55 nm and became ~ 46.26 nm at 400 °C with declined FWHM by ~ 13% than it was at 300 °C.

Comparing these results with the prior results of premelting Ni nanorods at 500 °C, it is observed that the intensity increasing in the Ni (111) continuous by that vein to reach ~ 2150 arb.

units in intensity at 500 °C which indicates the intensity change development by about 25% than it was at 400 °C. Moreover, the diameter was measured at 500 °C to be ~ 48 nm which means the increasing in diameter also happens as the temperature increases. However, the reduction of FWHM is noticed by ~ 9% than it was at 400 °C.

Furthermore, this study was extended by that vein at 600 °C. The results showed the drastic intensity change in the Ni (111) to be raised by ~123% which is a huge change that can provide the recrystallization and the formation of larger grains during annealing to form a new material with better crystals structures. Moreover, the Ni (111) at this temperature is considered the strongest and sharpest peak of all Ni (111) peaks at previous temperatures. The grain size increased slightly by 1.25 % than it was at 500 °C.

Moving to the Ni (200) peak, no significant change in intensity was observed until T = 500 °C. When the annealing temperature reached T ≥ 500 °C, the peak became sharper and stronger in intensity, narrower in width. XRD spectra indicate that the intensity change was increasing by ~ 134% at both temperatures 500 °C and 600 °C than the previous ones. These results also show the grain size increasing notably at these two temperatures by more than 50% than before to reach ~ 138.78 nm at 600 °C and ~ 138 nm at 500 °C. All XRD plots are displayed in FIG. 5.28, FIG. 5.29, and FIG. 5.30.

We can conclude from the discussion that Ni (111) shows the intensity increasing gradually during annealing at different temperatures starting with 300 °C leading to larger grain size as the temperature increases. However, no considerable change in intensity was observed in the peak of Ni (200) during annealing until reaching 500 °C and above. The massive intensity

change was observed which provides better grain size with new crystallization and formation of their structures.

Table 5.5: FWHM and average diameter on Ni (111) at different temperatures as calculated from Scherrer equation.

Ni nanorods with 90 min deposition	FWHM	Average diameter (*D*) (nm)
As-deposited	0.004	36.5
Annealed nanorods at T= 300 °C	0.0038	38.55
Annealed nanorods at T= 400 °C	0.0033	46.26
Annealed nanorods at T= 500 °C	0.003	48
Annealed nanorods at T= 600 °C	0.003	48.6

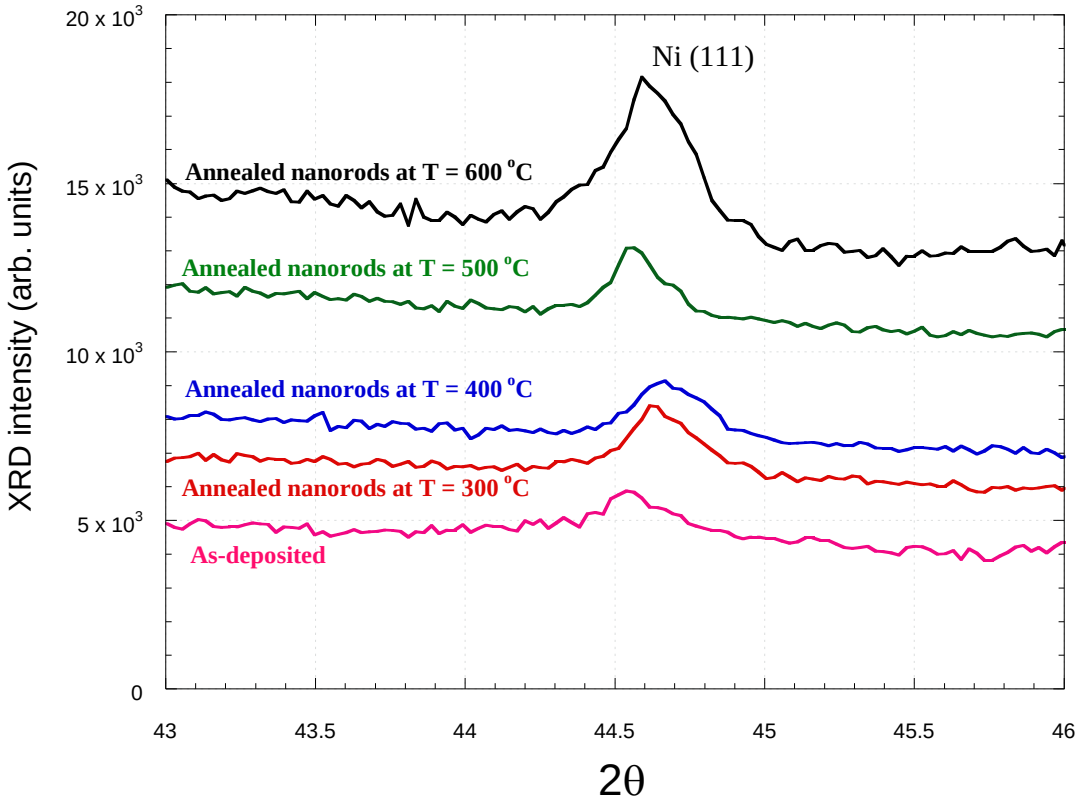

FIG. 5.28: Plot of Ni (111) peak at different temperatures.

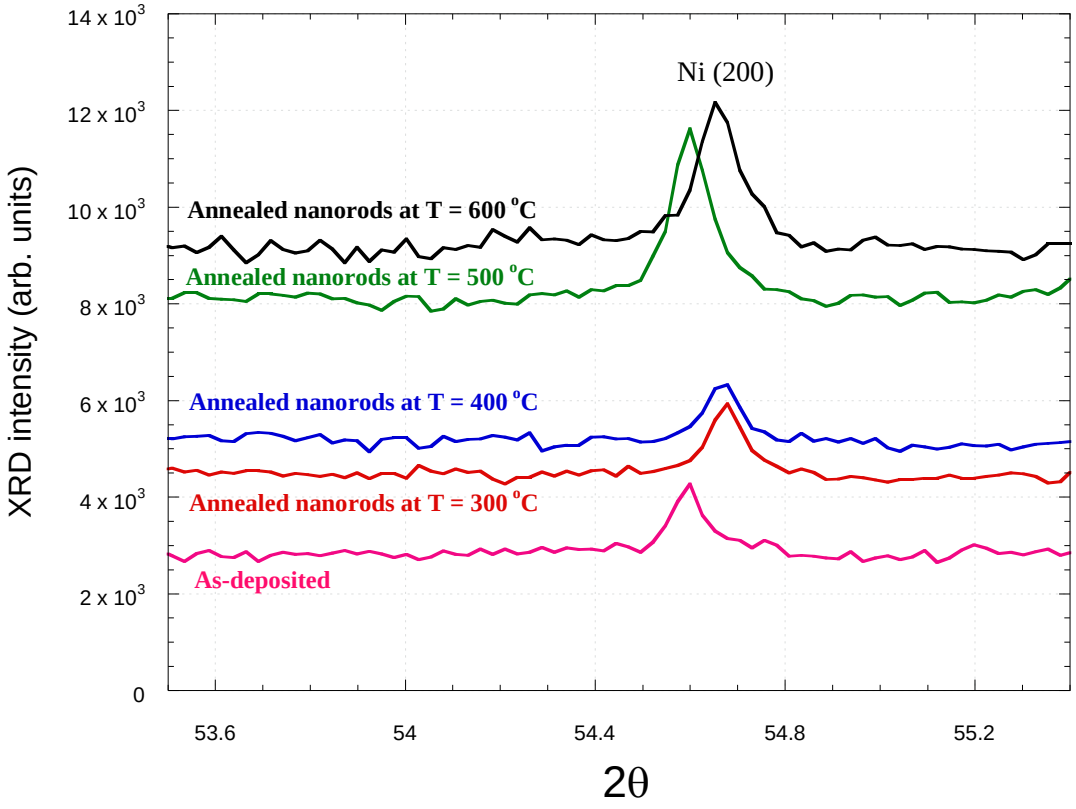

FIG. 5.29: Plot of Ni (200) peak at different temperatures.

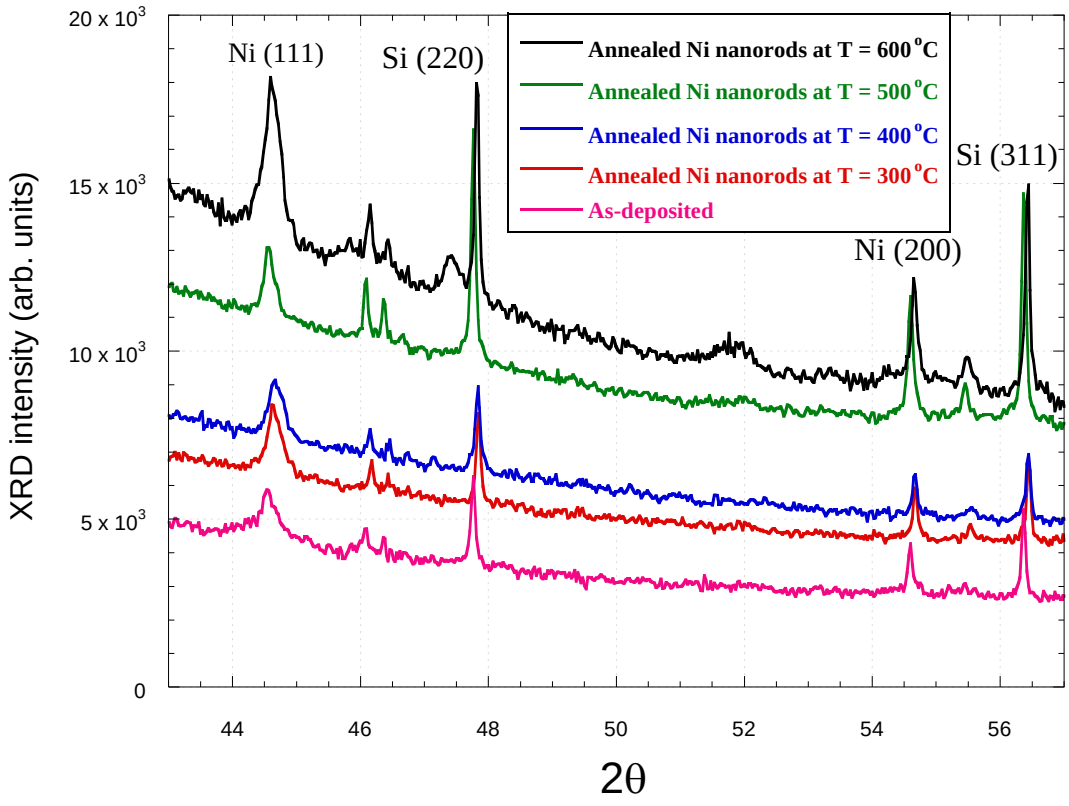

FIG. 5.30: Plot of both Ni (111) and Ni (200) peaks at different temperatures.

5.2.2 The Morphology Study of Temperature Dependent of Annealing Ni nanorod arrays:

In this study of our thesis, the annealing process was applied on the Ni nanorod arrays with 90 min deposition at different temperatures which were 300 °C, 400 °C, 500 °C, and 600 °C to study the change of the rods and their structures as the temperature increased. Other conditions in our experiments kept the same as before as mentioned in chapter 4. We started our study by annealing the sample at 300 °C. Then, the experiment was repeated for another Ni nanorod sample with 90 min deposition but at T = 400 °C. After that, the annealing process was reapplied on the sample with the same thickness at T = 600 °C. Hence, the results of these experiments were compared to the previous result of annealing Ni nanorods of 90 min deposition at T = 500°C.

As it is mentioned before that the as-deposited Ni nanorods is a huge group of columns with pentagonal prism body and pyramidal tip on each prism. These columns are separated by a spacing distance between them. These features of as-deposited Ni nanorods depict the wonderful roses on the surface of the substrate as it can be seen in the top view of SEM image in FIG. 5.31 but the cross sectional view of SEM image displays the columns as the leaves grown on the ground as appeared clearly in FIG. 5.26 (b). All these features of Ni nanorods are related to the nature nickel crystals.

After applying annealing process on our sample at T = 300 °C, no significant change in morphology on the rods is observed, just a slight difference is noticed whereas the columns started to tilt gradually to each other. Otherwise, the main features of the rods and their shape are still the same as before as shown in FIG. 5.32. The diameter of the rods is measured from SEM images and it is seen that the diameter of the columns has a drastic growing as the annealing

process stratified on the Ni nanorods at 300 °C. The particle size increased slightly from ~ 84 nm as-deposited to be around 106 nm after annealing at that temperature.

However, when the sample of Ni nanorods was annealed at 400 °C, the morphological changes on the rods appeared to be considerably more than at 300 °C. The rods started to loss some of their features such the edges of the rods began to curve and some of the rigorous features on the rods tips were perished to annealing which caused the columns to tilt to each other. Further, the nanorods appear to merge gradually to each other creating as groups of rods connected together. Thus, even for these observed changes, every column can be distinguished from another as displayed in the FIG. 5.33 According to those changes on the morphology our sample of Ni nanorods, it is assumed that the diameter of the rod also changed to be larger than before due to annealing at this temperature. It is measured from SEM images to be about 121 nm which was about 106 at 300 °C as shown in the Table 5.6.

Comparing these results with the previous result of premelting the sample of Ni nanorods with 90 min deposition at T = 500 °C that is shown in the previous section of this chapter, we can see the significant change of the nanorods features as increasing temperature. As mentioned before, it is obvious that the nanorods dramatically merge to each other more than the previous temperatures. Moreover, the columns coalesced to each other eliminating some gaps that separate each column from another and creating the pores between the groups of columns. Also, the rods lose some of their features such as the pyramidal tips due to the collapse of the rods originating the new formation of the Ni nanorod arrays. For the particle size, as it is measured before from SEM images, it raised at this temperature to reach 157 nm approximately which is the largest number of our Ni nanorods' diameters until now as shown in the Table 5.6.

In the last part of this study, the premelting process was applied to our sample at the high temperature of 600 °C with the same other conditions as before. The sample was tested by SEM to see the morphological changes and it is observed that the SEM images shows three different images of three different regions in the same sample as they are displayed in FIG. 5.35, FIG. 5.36, FIG. 5.37, and FIG. 5.38. These varies regions might be due to the stress in the sample that was constructed during annealing.

The first regime shows the substantial changes on the nanorods morphologies that the precise features of the rods disappeared due to annealing. It is seen that all columns appear with circle shapes on the top view SEM images which suggests that the columns convert to the cylindrical shapes without any tip on them and they fused to each other reducing the gaps between them. Further, as the new features of the columns appeared, little tiny webs started to originate due to annealing. The diameter on the Ni nanorods in this regime was undertaken from SEM images and it is about 160 nm which shows the increasing of particle size due to annealing.

The second regime of our sample displays that the rods amalgamated to each other more than the first part and the pores decreased between nanocolumns with the web features increasing over that change. It seems that the nanorods are completely changed to the new formation of the annealed Ni nanorod arrays under annealing the sample at 600 °C. Furthermore, it is become difficult to distinguish the dimensions of each rod because they melted to each other in groups.

The final part of that sample shows the huge changes on the morphology of the nanorods. They coalesce to each other strongly and form a denser film which correlated to the recrystallization and formation of larger grain which became difficult to measure in this stage due to their merging. Further, the pores between the nanorods shrink due to the coalescence of the rods to each other as increasing the temperature which suggests considering that vein of

study to control the pores in the nanorods surface in the future work. Moreover, the results indicate that the rods melt completely in this regime at this temperature. They collapse and fuse to each other in a new denser surface of nanorods due to the small gap between them. Thus, we can conclude this study to emphasize that the grain size of the Ni nanorods increases as the annealing temperature increased until the nanorods melt completely to deform a continuous denser film at high temperature such as 600 °C. However, the pores shrink and reduce as increasing temperature and that results can be considerable as a role of controlling pores by controlling the temperature applied on the Ni nanorods.

Table 5.6: The measured crystal size of Ni nanorods with 90 min deposition after annealing at different temperatures from SEM images.

Sample of Ni nanorods with 90 min deposition	The domain (crystal size) (*D*) (nm)
As-deposited	84 ± 10
Annealed Ni nanorods at T = 300 °C	106 ± 10
Annealed Ni nanorods at T = 400 °C	121 ± 10
Annealed Ni nanorods at T = 500 °C	157 ± 10
Annealed Ni nanorods at T = 600 °C	160 ± 10

SEM images of the second study of premelting Ni nanorod arrays

The samples were used in this study are the Ni nanorods with 60 min deposition at various temperatures:

- The Ni nanorods as-deposited with 90 min deposition:

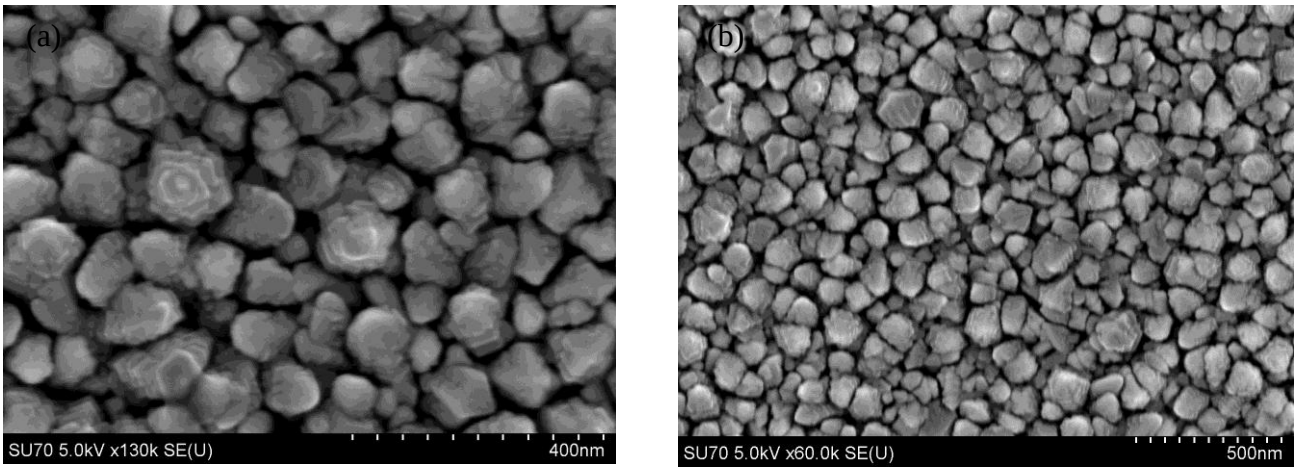

FIG. 5.31: SEM images of as-deposited Ni nanorods with 90 min deposition.
(a) The scale bar of the image is 400 nm. (b) The scale bar of the image is 500 nm.

- The annealed Ni nanorods at T = 300 °C:

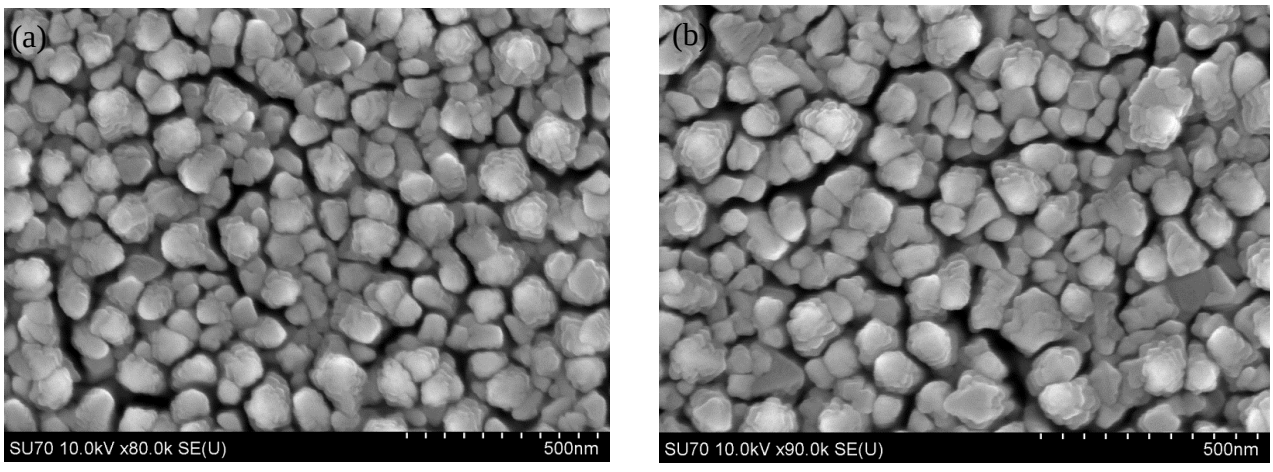

FIG. 5.32: (a) and (b) are SEM images of annealed Ni nanorods at T = 300 °C.

- The annealed Ni nanorods at T = 400 °C:

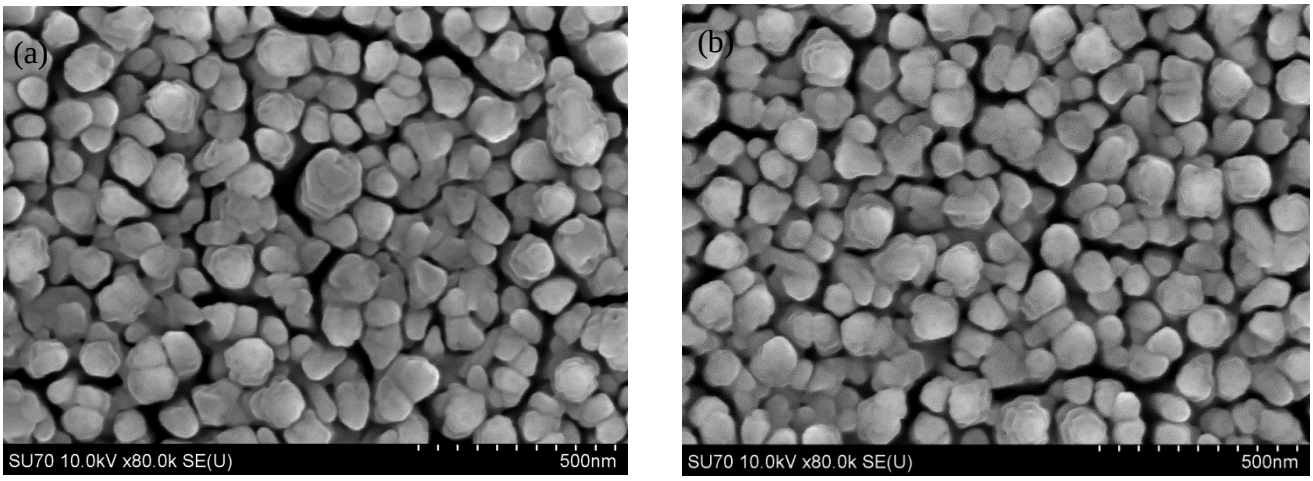

FIG. 5.33: (a) and (b) are SEM images of annealed Ni nanorods at T = 400 °C.

- The annealed Ni nanorods at T = 500 °C:

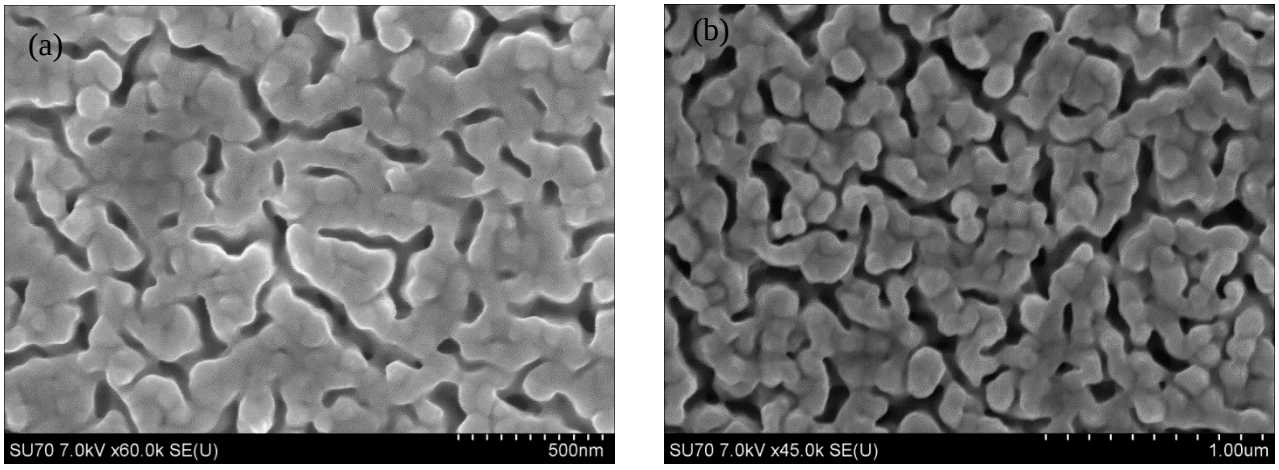

FIG. 5.34: (a) and (b) are SEM images of annealed Ni nanorods at T = 500 °C.
(a) The scale bar of the image is 400 nm. (b) The scale bar of the image is 500 nm.

- The annealed Ni nanorods at T = 600 °C:

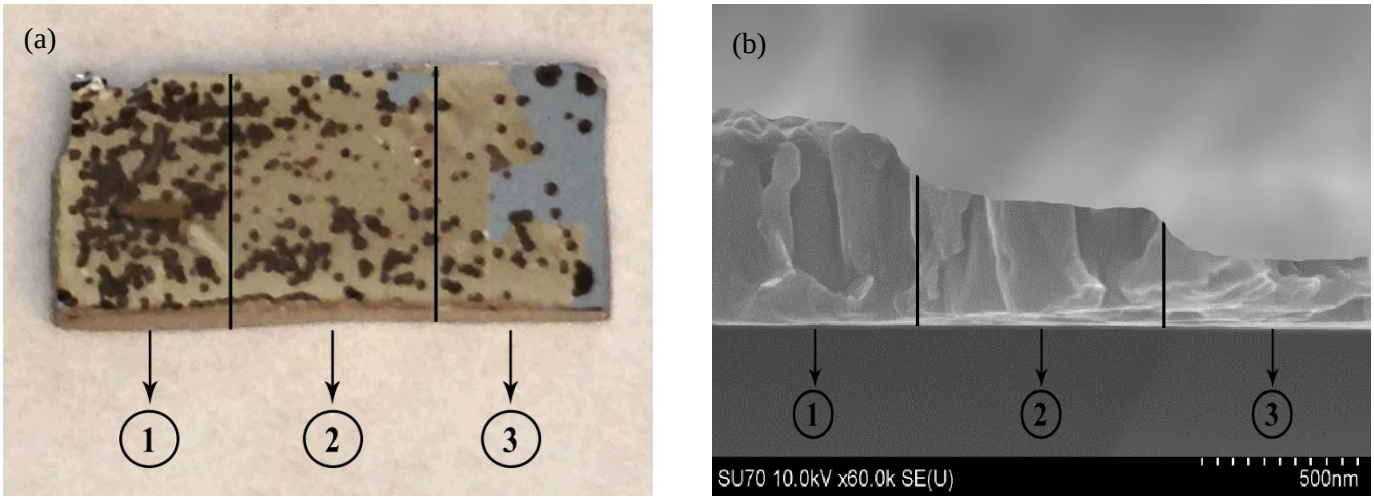

FIG. 5.35: (a) The illustrating figure of three regions on the top view of the annealed Ni nanorods at T = 600 °C. (b) The schematic cross-sectional view of the three regions.

1) The first region:

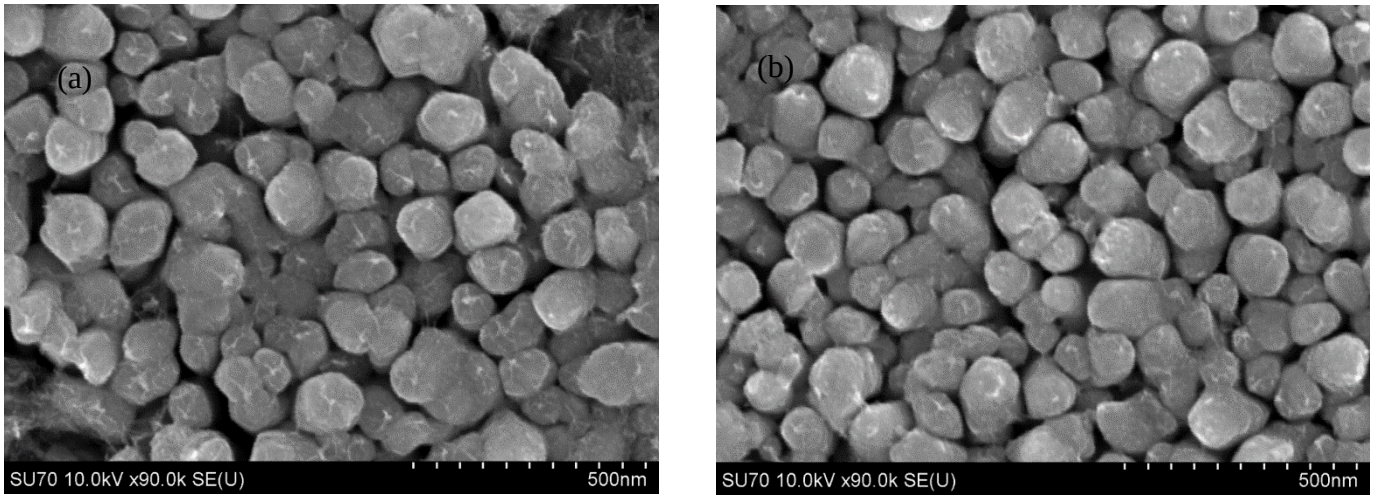

FIG. 5.36: (a) and (b) are SEM images of the first region of annealed Ni nanorods at T = 600 °C.

2) The second region:

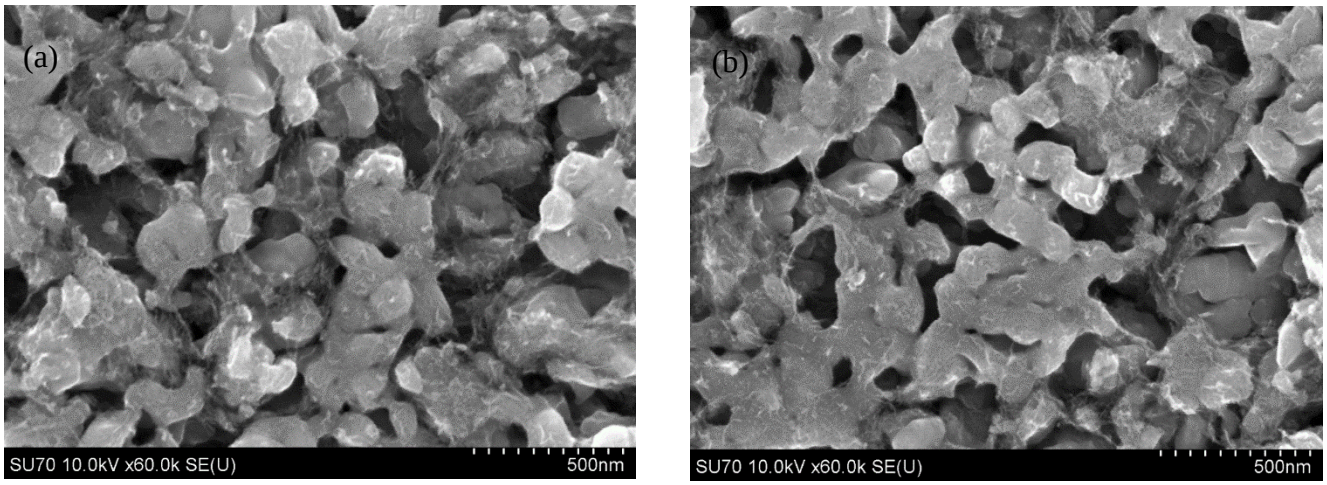

FIG. 5.37: (a) and (b) are SEM images of the second region of annealed Ni nanorods at T = 600 °C.

1) The third region:

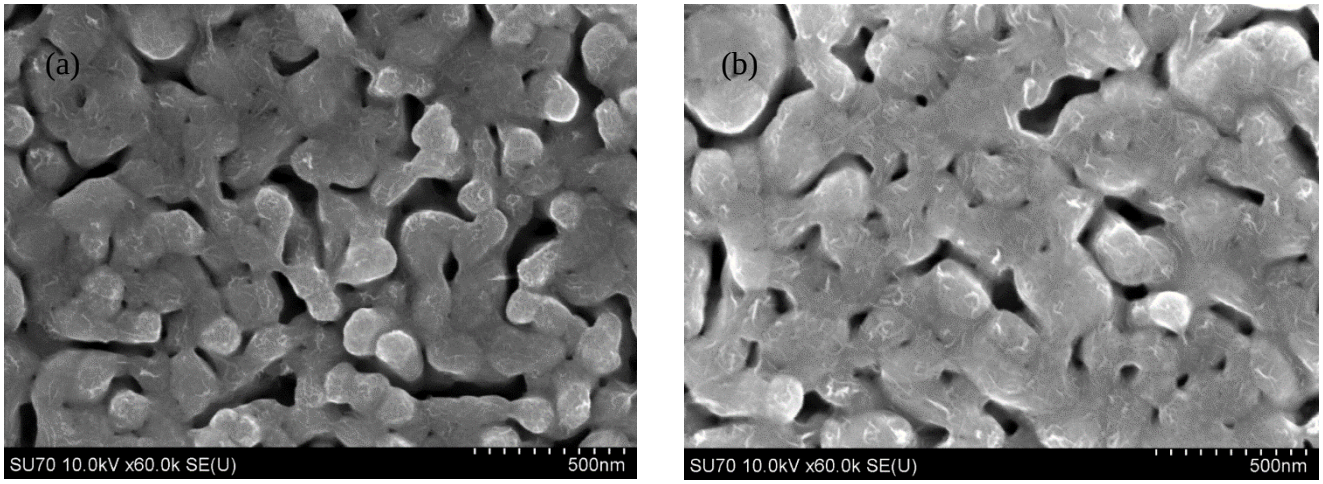

FIG. 5.38: (a) and (b) are SEM images of the third region of annealed Ni nanorods at T = 600 °C.

Chapter 6: Conclusions and Future Work

The study took an in depth look at various methods that are used to produce nickel nanorods of varying qualities. Additionally, nickel nanorods were successfully synthesized using the GLAD method. The role of annealing in changing the typography and properties of the nanocolumns was also examined. After annealing, the intensity of the peaks obtained using XRD increased for all the samples. For example, for nickel nanorods that had a 90 minute deposition time, the intensity increased by approximately 16400 arb. units. Using the Debye-Sherrer equation, the size of crystals produced using various methods was calculated. It is found that grain size increased with the size of a nanorod's thickness. Therefore, the longer the deposition period, the larger was the grain size of the sample. This shows that annealing simply allowed atoms to reorient themselves such that they formed larger crystals. The kinetic theory of matter might explain the observed behavior. Heating causes the particles to vibrate, allowing them to break some bonds, reorient and form larger crystals.

Images from SEM showed the structure of the resulting nanorods after annealing. A comparison of the images for the as-deposited and annealed samples showed that there was a considerable change in both their cross-sectional and top view of their morphology in SEM images. For example, the photo of the sample that was deposited in a 30 minute period had an almost particulate structure in the top view. The cross-section view shows a rugged arrangement of particles, with one being able to identify specific columns as they formed. Change in the sample that was annealed at a temperature of 500 °C was substantial. The top view shows that the particles moved closer together. Additionally, they are arranged is a specific way with most of the spaces that appeared in the as-deposited sample disappearing. In the cross-section view, the columns almost bonded completely, producing that image of a surface that has no spaces and

is almost solid. This was repeated in all the other samples, with the particles and columns becoming more arranged and leaving less space after annealing. This is especially apparent in the 90 minutes deposition sample.

Future experiments ought to investigate exactly what happens to the individual columns during annealing. How the changes in structure relate to temperature can be examined. Additionally, the properties of these changed materials after annealing could be looked at. This would provide greater insight into the behavior of nanorods, paving the way for greater application of the materials.

References

[1] *Nickel nanorods* (n. d.). Retrieved from http://www.americanelements.com/nimnr.html

[2] G. Singh, (2013, January 16). *Engineer making rechargeable batteries with layered nanomaterials.* Retrieved from http://www.k-state.edu/media/newsreleases/jan13/graphene11613.html

[3] H. Wang, C. M. B. Holtm, Z. Li, X. Tan, B. S. Amirkhiz, Z. Xu, B. C. Olsen, T. Stephenson, D. Mitlin, *Nano Research*, *5*, (2012), 605.

[4] M. F. Perutz, *Acta. Cryst.* A **46**, (1990), 633.

[5] W. L. Bragg, *Nature*, **90**, (1912), 410.

[6] W. L. Bragg, *Proceedings of the Cambridge Philosophical Society*, **17**, (1913), 43.

[7] W. L. Bragg, R. W. James, and CH. Bosanquet, *Phil. Mag.* **41**, (1921), 309.

[8] J. M. Robertson, *Br. J. Appl. Phy.* **14**, (1963), 635.

[9] W. L. Bragg, D. C. Phillips, and H. Lipson, "The Development of X- ray Analysis". (1992), New York: Dover. ISBN 0-486-67316-2

[10] R. J. Roe, "Methods of X- Ray and Neutron Scattering in Polymer Science". (2000), New York: New York. ISBN 0-19-511321-7

[11] F. P. Fewster, *Rep. Prog. Phys.* **59**, (1996), 1339.

[12] M. Birkholz, F. P. Fewster, and C. Genzel, " Thin- Film Analysis by X-Ray Scattering", (2006) Germany: Wiley- VCH Verlag GmbH & Co. KGaA, Weinheim, ISBN-13: 978-3-527-31052-4.

[13] B. D. Cullity and S. R. Stock, "Elements of X-ray Diffraction", (2001), Michigan, ISBN 0201610914, 9780201610918

[14] X- Ray Diffraction Primer 2001, Coastal and Marine Geology Program Online, Retrieved 25 February 2013, from http://pubs.usgs.gov/of/2001/of01-041/htmldocs/xrpd.htm

[15] S. Mitchell, J. Pérez-Ramírez, X-ray diffraction, Retrieved 1 March, 2013, from http://cc.usst.edu.cn/Download/26da9cdf-6134-41fc-bf56-6dcccd9edd20.pdf

[16] Bragg law 2013. *Encyclopedia Britannica Online*. Retrieved 25 February, 2013, from http://www.britannica.com/EBchecked/topic/76973/Bragg-law

[17] W. Massa, "Crystal Structure Determination", (2004), Springer- Verlag Berlin Heidelberg New York, ISBN 3-540-20644-2, PP. 4-5

[18] http://web.pdx.edu/~pmoeck/phy381/Topic5a-XRD.pdf

[19] http://en.wikipedia.org/wiki/Bravais_lattice

[20] A. Weibel, R. Bouchet, F. Boulc'h, and P. Knauth, *Chem. Mater*. **17**, (2005), 2378.

[21] http://cc.usst.edu.cn/Download/26da9cdf-6134-41fc-bf56-6dcccd9edd20.pdf

[22] M. T. Taschuk, M. M. Hawkeye and M. J. Brett, Glancing Angle Deposition. In Ed. P. M. Martin, *Handbook of Deposition Technologies for Films and Coatings*, 3rd Ed, (2010), 621.

[23] B. A. Movchan and A.V. Demchishin, *Fiz. Metal. Metalloved.* **28**, (1969), 653.

[24] M. M. Hawkeye and M. J. Brett. *J. Vac. Sci. Technol.* A **25**, (2007), 1317.

[25] B. Dick, M. J. Brett., T. J. Smy, M. R. Freeman, M. Malac, and R. F. Egerton, *J. Vac. Sci. Technol.*, A **18**, (2000), 1838.

[26] M. O. Jensen and M. J. Brett. *IEEE Trans. Nanotechnol*, **4**, (2005), 269.

[27] C. A. O. Yongzhi, W. U. Chao, H. U. Zhenjiang and Y. U. Fuli. (2013), 1.

[28] M. M. Hawkeye and M. J.Brett. *Adv. Funct. Mater*, **21**, (2011), 3652.

[29] S-Y. Hsu, C-H. Tsai and C-Y. Lu. *Organic Electronics*, **13**, (2011), 199.

[30] Y. He, Y. Zhao, *Phys. Chem. Chem. Phys*, **11**, (2009), 255.

[31] H. Ohnishi, Y. Kondo, and K. Takayanagi, *Nature (London)*, **395**, (1998), 780.

[32] C. L. Jackson and G. B. McKenna, *J. Chem. Phys.* **93**, (1990), 9002.

[33] L. J. Lewis, P. Jensen, and J. L. Barrat, *J. Phy. Rev.* B, **56**, (1997), 4.

[34] Z. L. Wang, J. M. Petroski, T. C. Green, and M. A. El-Sayed, *J. Phy. Chem.*, **102**, (1998), 32.

[35] I. Lisiecki, H. Sack-Kongehl, K. Weiss, J. Urban, and M.-P. Pileni, *Langmuir* **16**, (2000), 8807.

[36] S. Link, Z. L. Wang, and M. A. El-Sayed, *J. Phy. Chem*., **104**, (2000), 33.

[37] J. Wang, X. Chen, G. Wang, B. Wang, W. Lu, and J. Zhao, *Phy. Rev.* B **66**, (2002), 085408.

[38] B. Wang, G. Wang, X. Chen, and J. Zhao, *Phy. Rev.* B **67**, (2003), 193403

[39] T. Karabacak, J. S. DeLuca, and Pei-I Wang, G. A. Ten Eyck, D. Ye, G. Wang, and T. Lu, *J. Appl. Phy.* **99**, (2006), 064304.

[40] J. M. Nørgaard, N. B. Lorentzen, R. Petersen, and M. V. Madsen, (2007), "Growth of Nanostructures by Glancing Angle Deposition", Aalborg University – Nanotechnology, p. 6

[41] R. Behrisch and H. H. Andersen, (1981), "Sputtering by Particle Bombardment", Springer, Berlin; New York, ISBN: 0387105212

[42] M. Ohring, (2002), "Materials Science of Thin Films", Academic Press. p.215

[43] K. Robbie and M. J. Brett. *J. Vac. Sci. Technol.* A **15**, (1997), 1460.

[44] J. Chu, X. Peng, M. Sajjad , B. Yang, and P. X. Feng, *Thin Solid Films*, **520**, (2012), 3493.

[45] S. Y. Hsu, C. H. Tsai, C. Y. Lu, Y. T. Tsai, T. W. Huang, Y. H. Jhang, Y. F. Chen, C. C. Wu, and Y. S. Chen, *Organic Electronics*, **13,** (2012), 856

[46] www.wisegeek.com/what-is-an-annealing-furnace.htm

[47] A. L. Patterson. *Phys. Rev.* **56**, (1939), 978

[48] P. Wang, T. C. Parker, T. Karabacak, G-C Wang, and T-M Lu, *Nanotechnology* **20**, (2009), 085605.